

Fluorescence Enhancement of CdSe Quantum Dots with Au Nanocrystals

Melissa Aillaud

Bioengineering, University of California San Diego

NNIN REU Site: Nanoscience at the University of New Mexico

NNIN REU Principal Investigator: Ravi Jain, Electrical and Computer Engineering,

Center for High Technology Materials, University of New Mexico

NNIN REU Mentor: Li Wang, Electrical Engineering, Center for High Technology Materials, University of New Mexico

Contact: maillaud@ucsd.edu, jain@unm.edu, liwang@unm.edu

Abstract

Linear and nonlinear fluorescence were studied in cadmium selenium quantum dots (CdSe QDs) with gold nanocrystals (Au NCs). Linear photoluminescence measurements in CdSe QDs and Au NCs mixed solutions (1:1 and 5:1 mixing ratio by weight) showed significant fluorescence-intensity quenching effect, compared to a QDs-only sample. Another set of thin film samples gave over 3 times of enhancement in the nonlinear fluorescence measurement.

Introduction

Semiconductor QDs are nanoparticles with unique optical properties. Those properties, like large two-photon absorption coefficient, narrow emission and broad absorption spectra, and size-tunable fluorescence, have made them good substitutes for dyes that are typically used as fluorescent tags in biological applications. To understand and improve the QDs' efficiency in such applications, surface plasmon enhanced fluorescence was studied. The optical properties of small metal particles have been an attractive field of study for years, since they interact with incident light strongly and change the optical properties significantly. Such extraordinary properties can be explained by the excitation of coherent free electron oscillations, or surface plasmon polaritons. As a result of the high polarizability induced by such modes, a strong electrical field develops about the nanocrystals surface. This locally-enhanced electromagnetic field can be helpful to achieve enhanced fluorescence.

Materials and Experimental Design

We investigated the changes in fluorescence intensity for two sets of thin film samples. The first set is composed of

a monolayer of 5-nm-diameter CdSe QDs, a monolayer of 4.5 nm Au NCs and a separating section consisting of 4, 5, 14, 16 and 18 layers of polymethyl methacrylate (PMMA) to control the distance between the monolayers of QDs and NCs. The second set consists of a monolayer of 4.3 nm in diameter CdSe quantum rods (QRs) and the same monolayer of Au NCs. This set was assembled in a similar way as the first set, but using varying layers of amorphous silicon dioxide (SiO_2) to separate the QRs and gold monolayers. The setup of the linear fluorescence measurement is shown schematically in Figure 1. An argon laser was used to excite the sample, and the fluorescence was collected by two lenses and sent to a monochromator.

A photon-multiplier tube (PMT) and a lock-in amplifier were used to increase the sensitivity and signal-to-noise ratio of the setup. The nonlinear fluorescence measurement was done in a similar way except that: a mode-locked Ti-sapphire laser (wavelength ~ 800 nm, pulse width ~ 200 fs, repetition rate ~ 76 MHz and peak power > 10 kW) was used instead of the argon laser. Also to eliminate the loss introduced by the monochromator, we collected the fluorescence directly with a PMT.

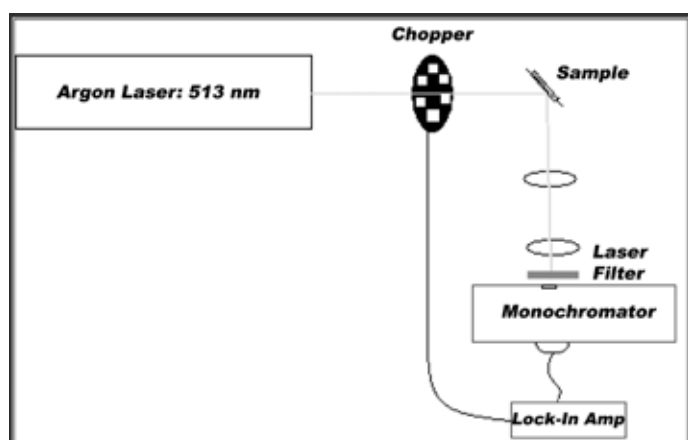


Figure 1: Schematic of linear experimental setup.

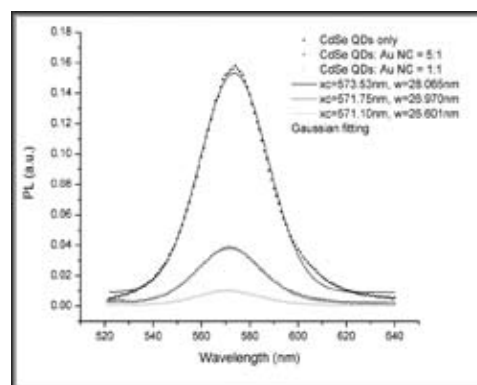


Figure 2: Photoluminescence intensities for samples in solution: Linear Experiment.

Results and Discussion

In the beginning, linear fluorescence measurements were done with QD/Au solutions mixed at different ratios: samples with QDs only, and QD/Au mixed at 1:1 and 5:1 ratios were compared. The results are shown in Figure 2. The QDs-only sample showed the strongest fluorescence, and the more Au NCs in the other two samples, the less fluorescence they gave. From the curve-fitting, we were not able to distinguish any significant center wave-length or full-width-at-half-maximum changes for all three samples tested. Although it seems to be quenching with more gold in the solution, the results are inconclusive since there are too many uncertainties, like re-absorption of fluorescence by Au NCs and uncontrollable spacing between QDs and NCs.

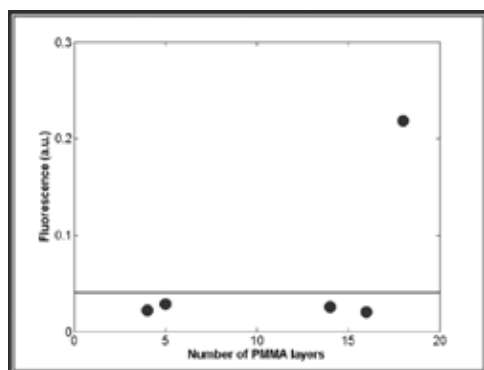


Figure 3: Average photoluminescence intensities for thin-film samples with PMMA: Linear Experiment.

Having this in mind, we obtained the QD/Au thin film samples which had the nanoparticles separated at “specific” distances using PMMA layering in between them. This batch of samples consisted of thin films with QDs only, and QDs and gold NCs separated with 4, 5, 14, 16 and 18 PMMA layers. We noted, though, that the samples had visible surface unevenness, which is why, during the linear and nonlinear experiments, we decided to scan through the sample with the laser and obtain an average of the intensities. For the QD/Au thin film samples with PMMA layering, Figure 3 shows the average of the fluorescence intensities for varying PMMA layers in the linear experiment. The red line represents the average intensity for the QDs-only sample. From the intensity plots generated with the fluorescence data obtained, there is no significant fluorescence quenching or enhancement in these samples.

The 18-layer PMMA sample seems to be totally different from others, and we believe that there might have been some mistakes during fabrication (possibly the PMMA layers folding upon themselves). Figure 4 shows the data obtained for the nonlinear

fluorescence experiments on the same samples with PMMA layering. Without considering the 18-layered sample, over 3-fold of fluorescence enhancement has been observed in the 4-layered sample compared with the CdSe QDs only sample (red line). Furthermore, the optimum spacing seems to be smaller than 4-layered thickness. To further investigate the optimum spacing between the CdSe QDs and Au NCs, thinner and more precisely controlled layers are needed.

The final set of samples consisted of QR/Au thin films fabricated more precisely with SiO₂ layering to separate the nanoparticles from each other. The surface of the samples was much more even than the previous set of samples; unfortunately, we could not perform the planned experiments because of laser malfunction.

Conclusions and Future Work

We have shown that over 3-fold of nonlinear fluorescence enhancement in CdSe QDs monolayer with Au NCs can be obtained. Future work will be done with the last set of samples when the laser is available, but similar results are expected for the nonlinear experiments. Once this is done, we will be able to calculate the optimal distance between the nanoparticles and fabricate the QD/NC particles so that they can be used in biological applications.

Acknowledgements

I would like to acknowledge and give special thanks to Prof. Ravi Jain and Li Wang. Also, thanks to our collaborators in Prof. Brinker’s lab; Robert Bradley and Shisheng Xiong. Special thanks to the National Nanotechnology Infrastructure Network Research Experience for Undergraduates Program and National Science Foundation for funding my participation in this project. Muchas gracias a mi familia.

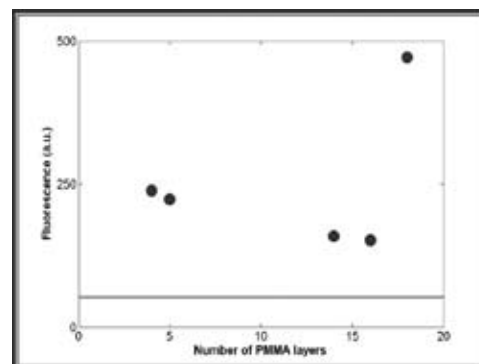


Figure 4: Average photoluminescence intensities for thin-film samples with PMMA: Non-linear Experiment.

Manipulation of Iron Nanoparticles and Their Effects on Human Colon Carcinoma Cells

Ebony Ayres

Pharmacy Practice/Pharmaceutical Sciences, Hampton University

NNIN REU Site: Howard Nanoscale Science and Engineering Facility (HNF), Howard University

NNIN REU Principal Investigators: Dr. Gary L. Harris and Dr. Winston Anderson, HNF, Howard University

NNIN REU Mentor: Nefertiti Patrick-Boardley, Applied Physics, University of Michigan

Contact: ebony.ayres@pipeline.hamptonu.edu, gharris@msrce.howard.edu

Abstract

Magnetic nanoparticles (MNPs) were synthesized to evaluate the influence of various polymer coatings on particle size, zeta potential, and cellular uptake. Stock solutions of gum arabic (GA), chitosan, and polyethylenimine (PEI) at 2% by weight were added to the MNP solutions. The particle size was obtained with the vibrating sample magnetometer and Malvern Zetasizer. The coated particles were on average approximately 100 nm. The zeta potential of the particles was acquired with the Malvern Zetasizer. Results revealed a negative surface charge for each of the coatings at low concentrations. Increased amounts of PEI demonstrated the ability to alter the surface charge from negative to positive. The live/dead (LD) assay showed that PEI coated particles demonstrated toxic effects with a LD 50 \approx 100 μ g iron/millions cells. In contrast, GA and chitosan-coated MNPs were the least toxic to the human colon carcinoma cells (HCT-166) with a LD 50 > 1000 μ g iron/millions cells. Being non-toxic is important because it relates the biocompatibility of the nanoparticles with the body system.

Introduction

Colon cancer is one of the most prevalent and fatal types of carcinoma disease [1]. There are several studies dedicated to optimizing cancer therapy through the use of nanotechnology applications [2]. Magnetic field hyperthermia (MFH) makes use of MNPs, such as magnetite. When coated in glycomolecules, like GA and chitosan, a crab shell derivative, it is thought that MNPs are more likely to be taken up by cancer cells than by healthy cells because cancer cells require more energy to proliferate. Also, because cancer cells are negatively charged, it's interesting to note whether surface charge affects particle uptake across the cell membrane's phospholipid bilayer. With an accumulation of MNPs in or around cancerous cells, an alternating magnetic field (AMF) causes hysteresis heating. Hysteresis heating around 42°-45°C leads to the apoptosis of cancerous cells while leaving healthy cells unharmed [3].

However, MFH is most effective if the MNPs are at an optimal size, concentration, adhesiveness, and strength. The goals of this experiment were to manipulate the physical and chemical surface properties of magnetic nanoparticles (MNPs) by coating them with polymer and to evaluate how these polymers influence surface charge. Additionally, we sought to determine the cell viability when exposed to polymer-coated MNPs.

Methods/Materials

The MNPs were synthesized via wet chemistry techniques. A 2:1 molar solution of iron (III) chloride and ferrous chloride was added to 20 mL of deionized water. An alkaline solution was prepared by adding 15 mL of reagent NH_4OH to 65 mL of

deionized water. The latter solution was stirred for approximately 5 minutes on a magnetic stir plate. The Fe^{2+} , Fe^{3+} solution was added drop-wise to the alkaline solution. It is believed that pouring the iron solution into the alkaline solution would result in smaller particles; however a slower reaction rate correlates with more uniform particles. The MNP solution was stirred for 1 hour and washed via centrifugation. The MNPs were redispersed with deionized water via ultrasonication. This process was repeated about six times or until the pH of the suspension was comparable to that of the deionized water. The polymer-coated MNPs were synthesized via the same method with the addition of 2% polymer solution after ultrasonication.

Overall, four types of MNPs were used: naked, chitosan-coated, GA-coated, and PEI-coated. The Malvern Zetasizer was used to measure size and zeta potential. Size measurements were verified via magnetic susceptibility analysis. A live/dead cell assay was performed with each particle type at concentrations from 31-8000 μ g iron/million cells.

Results and Discussion

Size analysis via vibrating sample magnetometer and dynamic light scattering (Malvern Zetasizer) showed that the naked particles were 3.84-60.4 nm. The smaller sizes represent primary particles, and the larger sizes represent agglomerates. The coated particles were about 100 nm. Zeta potential results, which correlate with electrophoretic mobility, showed that the nutrient medium for cells (DMEM) in which the particles were suspended for testing rendered all the particles negatively charged. PEI had

the strongest negative charge at -6.9 mV. It was interesting to note that PEI and chitosan-coated MNP's exhibited a negative charge in DMEM even though PEI and chitosan are cationic polymers. The live/dead cell assay showed that the LD 50 results for GA, chitosan, and PEI were 6700, 1450, and 106 μg iron/millions cells, respectively (see Figure 1).

The particle size retrieved via the two size analysis techniques gave size measurements which were consistent with predicted and literature results. The MNPs were tested in DMEM solution to more accurately simulate the body system. In this solution, all the coatings, even those which are typically positively charged, rendered a negative surface charge. The PEI coated MNPs were very toxic to the cells at higher concentrations, which could cause rejection if used in the human body. Although chitosan particles were promising in relation to their biocompatibility, GA best reflected the live/dead cell assay results of particles with no coatings.

Summary

Polymer-coated MNPs imparted an overall negative charge. The live/dead cell assay showed that overall GA was the least toxic to the colon carcinoma cells meaning that it would be the most biocompatible. Further studies need to be done to identify and optimize surface coatings that could render a positive surface charge. Additionally, particle uptake of the coated MNPs needs to be observed via TEM imaging.

Acknowledgments

I would like to thank my PIs, Dr. Gary L. Harris and Dr. Winston Anderson, my mentor, Nefertiti Patrick-Boardley, Dr. Otto C. Wilson, Dr. Patrick Mehl, HNF staff, National Nanotechnology Infrastructure Network REU Program, and the National Science Foundation for their efforts and support.

References

- [1] National Cancer Institute. Colon and Rectal Cancer Homepage. <www.cancer.gov/cancertopics/types/colon-and-rectal>.
- [2] Cuenca A., Jiang H., et al. Emerging Implications of Nanotechnology on Cancer Diagnostics and Therapeutics. Wiley Interscience 2006: 459.
- [3] Ivkov R., DeNardo S., et al. Application of High Amplitude Alternating Magnetic Fields for Heat Induction of Nanoparticles Localized in Cancer. Clin Cancer Res 2005; 11 (19 Supply): 7093s.

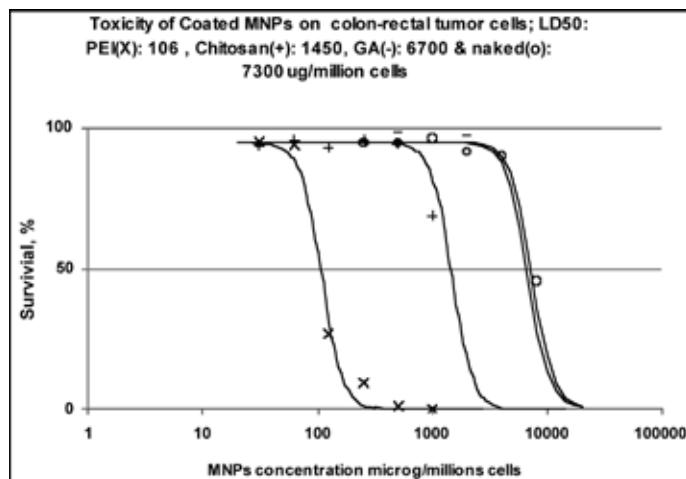


Figure 1: LD 50 chart obtained from live/dead cell assay.

Fabrication of Multifunctional Atomic Force Microscopy-Scanning Electrochemical Microscopy Probe Arrays

Brian Bolz

Electrical Engineering, Manhattan College

NNIN REU Site: Microelectronics Research Laboratory, Georgia Institute of Technology

NNIN REU Principal Investigators: Dr. Christine Kranz and Dr. Boris Mizaikoff,

Chemistry and Biochemistry, Georgia Institute of Technology

NNIN REU Mentor: Dr. Heungjoo Shin, Chemistry and Biochemistry, Georgia Institute of Technology

Contact: bbolz.student@manhattan.edu, christine.kranz@chemistry.gatech.edu, gt7018b@mail.gatech.edu

Abstract/Introduction

Combined atomic force scanning electrochemical microscopy (AFM-SECM) probes integrated with micro/nano-electrodes enable simultaneous collection of electrochemical information along with high resolution topological imaging [1-3]. Thereby, an innovative technique for correlating surface chemical activity and topography during a single sample surface scan is provided. In the present research, a batch fabrication process at the wafer level was developed for incorporating an array of four AFM-SECM cantilevers with recessed electrodes. The electrode was located at a defined distance from the tip apex enabling separation of correlated topographical and electrochemical information. The bifunctionality of the individual probes is demonstrated by AFM imaging and electrochemical characterization of the integrated electrodes.

The presented development was at the forefront of combined scanning probe technology providing sub-microelectrode integrated AFM probe arrays for the first time.

Fabrication

Multifunctional cantilever arrays were fabricated from a 4" silicon-on-insulator (SOI) wafer consisting of a device layer of 10 μm silicon (Si), a stop etch layer of 1 μm silicon dioxide (SiO_2) and a handle layer of 500 μm Si. This procedure is conducted using a batch process involving the development of over three hundred microchips on a single wafer. Each microchip contains four gold (Au) pad openings and four cantilevers of various heights and widths.

First, the device silicon layer AFM tips were fabricated using an isotropic reactive ion etching (RIE) process. The AFM tip surface was insulated by a 500 nm plasma enhanced chemical vapor deposition (PECVD) silicon nitride (SiN) layer. An etch mask for backside Si etch was patterned by successive 6 μm PECVD SiO_2 layer deposition and wet etching. The electrode layer is then patterned using lift-off process of 100 \AA titanium and 2000 \AA gold deposited using an e-beam evaporator. Another 500 nm PECVD SiN layer insulated the metal layer. Four gold pads were exposed by an RIE process for electrical connection to individual electrodes for electrochemical measurements. Each cantilever profile was defined by etching the SiN and the silicon device layers with RIE and inductively coupled plasma (ICP) etching processes respectively. The backside of the microchip was then etched through ICP. Each cantilever chip was then removed from the host wafer and focused ion beam (FIB) technology was used to open each tip electrode and shape the AFM tip [1].

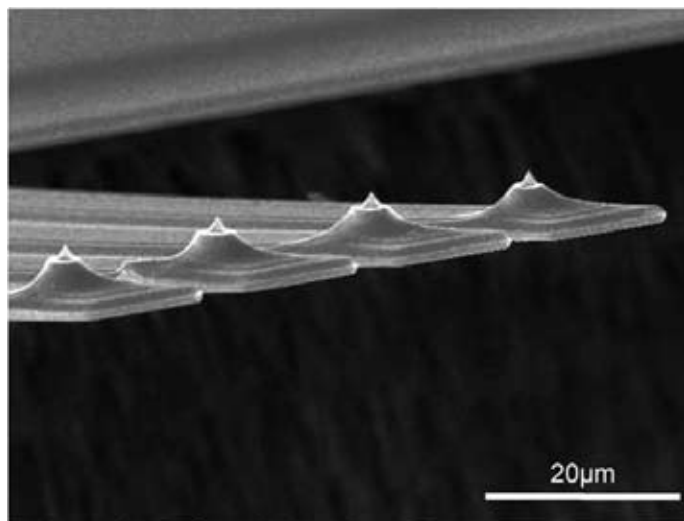


Figure 1: SEM image of a fabricated AFM-SECM probe array.

Results and Conclusions

An AFM-SECM probe array is shown in Figure 1. Each cantilever chip contains four separate cantilevers with 20 μm or 16 μm spacing between each tip apex. The imaging quality of the cantilever was tested.

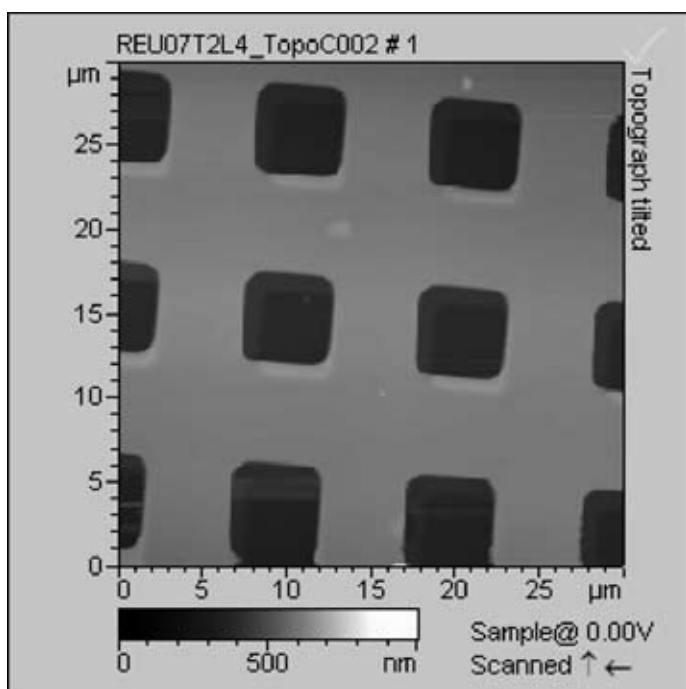


Figure 2: AFM of a test grid recorded with a single cantilever from the array.

The AFM laser was focused on one of the cantilevers and scanned across a model sample; the AFM image is shown in Figure 2. The change in color along the lower edge of each etched region is related to the spot size of the used laser, which results in an overlapping readout of two neighboring cantilevers.

The electrochemical functionality of the cantilever array was then tested by cyclic voltammetry (CV) in 0.1 mol/L $K_4Fe(CN)_6$ in 0.5 mol/L KCl in a potential range from 0V-0.6V. CVs were recorded before and after focused ion beam (FIB) milling (Figure 3). As shown in the voltammograms, the current level before tip milling is in the low pA range, which indicates good insulation. The same test was then conducted after tip milling. The measured steady state current of 1.68 nA is in good agreement with the expected theoretical value for the given electrode size.

Finally the free vibration of the cantilever in air was recorded and the spring constant of the cantilevers was calculated to be 0.95-1.2 N/m which is comparable to that of commercial cantilevers. The frequency response of the cantilevers in air was also conducted using a mean-square displacement which verified that the AFM-SECM cantilevers have a resonant frequency of 69.1 kHz, also comparable to commercial cantilevers [1].

In conclusion, the first known AFM-SECM integrated probe array was successfully fabricated using microfabrication techniques suitable for production on a wafer level. The gold microelectrodes were integrated recessed from the tip apex allowing simultaneous topographical and electrochemical imaging. The AFM-SECM cantilever performance as AFM cantilevers was verified and is comparable to that of commercial cantilevers and electrochemical functionality was demonstrated by cyclic voltammetry.

Future Work

Simultaneous topographical and electrochemical imaging will be demonstrated with one of the four cantilevers of the array. Parallel readouts from each cantilever are anticipated in the future with a modified AFM set-up. Reducing the size of the integrated microelectrode will result in improved resolution for electrochemical imaging. Ultimately, individual modifications of each electrode of the cantilever array with biosensing layers or pH sensing layer will allow multiple parameter readouts during AFM imaging.

Acknowledgements

I would like to thank Dr. James Meindl, Jennifer Root, and the staff at MiRC for providing a pleasant work environment. Also thanks to my mentor Dr. Heungjoo Shin for his close work, and Christine Kranz and Boris Mizaikoff for providing the topic for the research project. Finally, I would like to recognize the National Nanotechnology Infrastructure Network REU Program and the National Science Foundation for their funding and support during this project.

References

- [1] C. Kranz, G. Friedbacher, B. Mizaikoff, A. Lugstein, J. Smoliner, E. Bertagnolli, "Integrating an Ultramicroelectrode in an AFM Cantilever: Combined Technology for Enhanced Information"; *Anal. Chem.*, 73, 2491, (2001).
- [2] A. Lugstein, E. Bertagnolli, C. Kranz, A. Kueng, B. Mizaikoff, "Integrating micro- and nanoelectrodes into AFM cantilevers using FIB techniques"; *Appl. Phys. Lett.*, 81, 349 (2002).
- [3] H. Shin, P. Hesketh, B. Mizaikoff, C. Kranz, "Batch Fabrication of AFM Probes with Recessed Integrated Ring Microelectrodes at a Wafer Level"; *Anal. Chem.*, 79, 4769-4777, 2007.

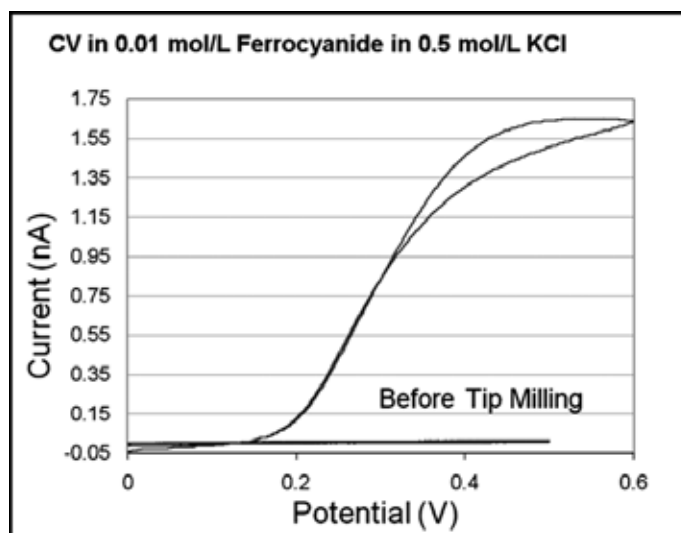


Figure 3: CV recorded at the integrated electrode of the cantilever.

Utilization of Surface Acoustic Waves for On-Chip Manipulation of Micro/Nano Particles

Ashley Colletti

Biomedical Engineering, The Johns Hopkins University

NNIN REU Site: Penn State Center for Nanotechnology Education and Utilization, The Pennsylvania State University

NNIN REU Principal Investigator: Dr. Tony Jun Huang, Engineering Science and Mechanics, The Pennsylvania State University

NNIN REU Mentors: Jinjie Shi and Xiaole Mao, Engineering Science and Mechanics, The Pennsylvania State University

Contact: ashleycolletti@jhu.edu, junhuang@psu.edu, jus239@psu.edu, xum101@psu.edu

Abstract

The on-chip integration of microfluidic and surface acoustic wave (SAW) systems provides a promising platform for potential applications such as cell patterning, cell sorting and separation, high throughput screening in drug development and testing, and ultrafast mixing. In this study, we integrated polydimethylsiloxane (PDMS) microchannels with interdigitated transducers (IDTs) on a piezoelectric substrate to enable the on-chip manipulation of micro/nano particles. Photolithography techniques were utilized to define the micropattern for both the microchannels and IDTs. The mold for the PDMS microchannels was fabricated via deep reactive ion etching (DRIE) on a photoresist-patterned silicon (Si) wafer. Precision control of polystyrene (PS) micro/nano particles is achieved by generating standing SAW within the microchannel using IDTs. Through careful arrangement of microchannels and IDTs, one-dimensional and two-dimensional patterning of micro/nano particles in the microchannel can be achieved.

Introduction

In recent years, much interest has been expressed in the development of robust, integrated lab-on-a-chip systems which serve a multitude of purposes in engineering, medicine, and biochemistry. In this study, our goal was to design, fabricate, and test an on-chip integrated microelectromechanical systems (MEMS) device that would enable aggregation of micro/nano particles within a microchannel at the pressure anti-pressure nodes of standing SAW.

Microfluidic channels provide a controlled region for study, taking advantage of laminar flow, low Reynolds numbers, and high surface area to volume ratios [1]. The underlying mechanism

for particle patterning stems from wave theory, where two approaching waves converge and undergo positive interference to form standing waves. In this project, a piezoelectric substrate was used due to the fact that it functions as an energy interface, converting between electrical and mechanical forms of energy. Thus, when a form of electrical energy, voltage, is applied across an electrode on a piezoelectric substrate, mechanical vibrations of the substrate result, and SAW propagate across the medium, perpendicular to the IDT. Arranging two IDTs in either parallel or angled patterns enables precise 1D or 2D patterning, respectively, at the pressure nodes of the standing SAW.

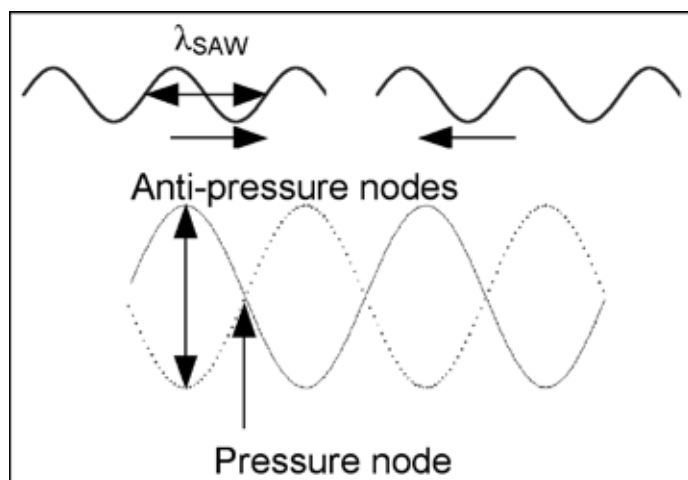


Figure 1: The underlying mechanism for particle manipulation: the combination of two converging SAWs into one standing SAW.

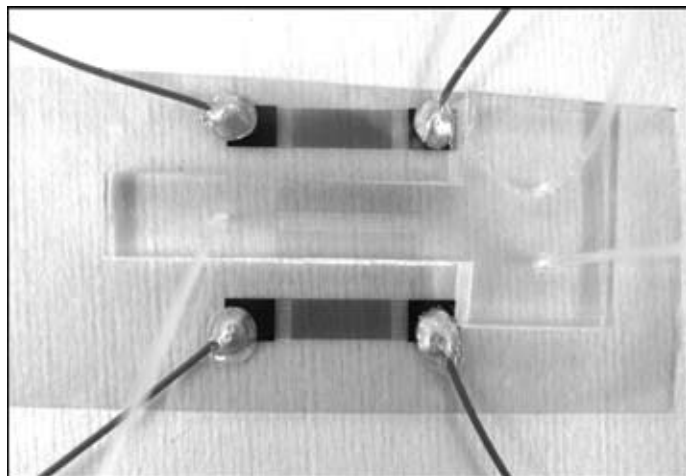


Figure 2: On-chip combined acoustic and microfluidic systems: titanium/gold IDTs with wires bonded and PDMS microchannel with polyethylene tubing, ready for testing.

Experimental Procedure

Photolithography techniques were implemented in both the fabrication of the IDTs and microchannels. First, IDT and microchannel masks considering a variety of parameters were designed on AutoCAD. Based on the orientation of the IDTs and microchannels, both 1D and 2D patterning systems were designed.

Both masks were written on a laser writer, and contact lithography was used for the patterning of the Si wafer for the microchannel mold and the piezoelectric IDT substrate. Following, the photoresist-patterned Si wafer underwent DRIE, which etched into the exposed areas of the wafer, creating a Si mold for microchannels. PDMS was mixed and poured over the mold and cured, and the microchannels were released. To complete the IDT fabrication, an adhesive layer of titanium (Ti) was deposited, followed by a layer of gold (Au), by metal evaporation onto the photoresist patterned piezoelectric substrate. Finally, the Ti/Au electrodes were revealed by a chemical liftoff process, removing any remaining photoresist/Ti/Au.

Device integration challenges were overcome by relying on reactive ion etching (RIE) to pre-treat bonding surfaces of both the PDMS microchannel and piezoelectric substrate. Immediately following low-power oxygen RIE, microchannels were aligned with the IDTs under a microscope. Wires were bonded to the IDT electrodes, and polyethylene tubing was inserted into the microchannel inlets and outlets.

The device testing experimental setup consisted of an radio frequency (RF) signal generator first connected to a power amplifier, which was then connected to both IDTs. An oscilloscope recorded the signal voltage and frequency. The integrated MEMS device was placed on the stage of an inverted optical microscope for testing. Specified flow rates of micro/nano particle containing fluid were delivered to the polyethylene tubing by a syringe pump.

Results and Conclusions

In conclusion, we have developed an effective method for the on-chip manipulation of micro/nano particles. When an alternating current (AC) signal was applied across the surface of both IDTs, aggregation of micro/nano particles within the

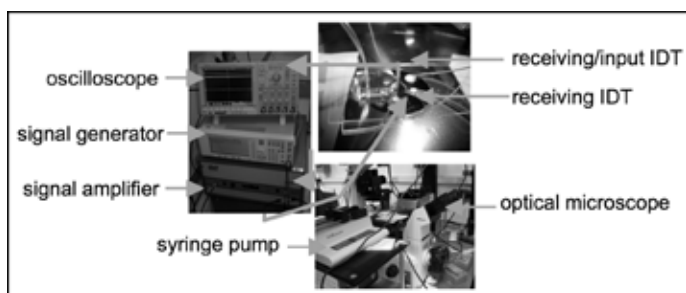


Figure 3: Experimental setup consisting of signal generator, power amplifier, MEMS device, syringe pump, inverted optical microscope, and oscilloscope.

microchannels did occur successfully at the pressure nodes of the standing SAW. Both 1D and 2D patterning of micro/nano particles was achieved, resulting in an aggregated line or grid of dots, respectively. Patterned particles ranged in size from 460 nm to 10 μm in diameter.

Future Work

This work boasts a multitude of applications, particularly in pharmaceuticals, biology, and biochemistry. Future work involving the patterning of cells would be applicable to drug discovery, development, and testing. This technique could potentially be used to affix the positions of cells and provide a uniform environment for monitorable testing during high throughput screening. Cell responses to variations in dosage amount, frequency, and other factors could be observed. Secondly, functionalizing molecules with polystyrene micro or nano particles could lead to improvements in molecular sorting and deoxyribonucleic acid (DNA) analysis techniques. Finally, microfluidic in-channel mixing, which is often difficult to attain in laminar microfluidic systems, could be achieved efficiently by selective functionalization and patterning of molecules.

Acknowledgements

The author wishes to thank Dr. Tony Jun Huang, Jinjie Shi, and Xiaole Mao of the Penn State Bio-NEMS Group for their support and motivation throughout the project, the Penn State Nanofabrication Facility and staff for assistance and patience with fabrication, and the Penn State Center for Nanotechnology Education and Utilization and the National Nanotechnology Infrastructure Network Research Experience for Undergraduates Program for this incredible opportunity. She would also like to thank the NNIN and NSF for funding.

References

- [1] Squires, T. M., Quake, S.R.; "Microfluidics: Fluid physics at the nanoliter scale; Revs of Modern Physics, 77, 977-1026 (2005).

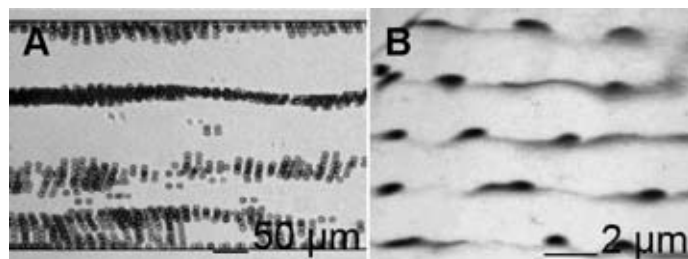


Figure 4: 1D patterning of 10 μm (A) and 2D patterning of 1 μm (B) polystyrene microparticles at pressure nodes of standing SAW.

(Note new publication; "Focusing Microparticles in a Microfluidic Channel with Standing Surface Acoustic Waves"; J. Shi, X. Mao, D. Ahmed, A. Colletti, and T.J. Huang. Received 1st January 2007, Accepted 1st January 2007, First published on the web, 1st January 2007, www.rsc.org/loc | Lab on a Chip.

Novel Optical Trapping Particles for Biological Experiments

Nathan Friez

Applied Physics, Bethel University

NNIN REU Site: Cornell NanoScale Science & Technology Facility, Cornell University

NNIN REU Principal Investigator: Dr. Michelle Wang, Physics, Cornell University

NNIN REU Mentors: Dr. Chris Deufel and Scott Forth, Physics, Cornell University

Contact: frinatm@bethel.edu, mdw17@cornell.edu, cd77@cornell.edu, sf73@cornell.edu

Abstract

Optical trapping is a powerful technique used to investigate the mechanical properties of the molecular motors that govern cellular processes. In order to examine such mechanisms, trappable “handles” must be developed that can be used for attachment to biological samples. This project involves the design and fabrication of cylindrical trapping particles to be used in measuring forces and torques exerted on deoxyribonucleic acid (DNA), in addition to optimizing existing fabrication protocols. In previous work, the entire top surface of a cylinder was chemically functionalized for binding to DNA. During the first stage of this project, this protocol was repeated with slight modifications in order to generate cylinders which dramatically reduced the unwanted precessing of particles in an optical trap, thereby minimizing measurement noise. The second stage principally dealt with fabricating smaller cylinders (600 nm height, 300 nm diameter) to allow for more accurate and precise measurements. Progress in this area has proved challenging, likely due to having approached the optical limits of the nanofabrication tools being used. It may ultimately prove more beneficial to design and fabricate a new type of trapping particle.

Introduction

There have been a myriad of uses for optical traps in the field of single molecule biophysics, with special emphasis on systems involving DNA. Briefly, an optical trap can be described as an instrument that uses collimated light, normally provided by a single mode laser, which is brought into a tight focus by high numerical aperture (NA) objective lenses to trap dielectric particles. The principal forces involved in an optical trap are the scattering force (a result of the momentum of photons) and the gradient force, which is the force that actually does the trapping. The scattering force “is proportional to the light intensity and acts in the direction of the propagation of light” while the gradient force is “proportional to the spatial gradient in light intensity and acts in the direction of that gradient” [1]. The diameter of the particles is on the order of the wavelength light that is being used.

In this project we used crystalline quartz, which is birefringent, as our substrate for fabricating cylindrical trapping particles in order to make measurements of torque and force on DNA in an angular optical trap. In addition to being a well understood fabrication material, quartz was used since “angular trapping occurs in particles made from materials such as quartz, in which the extraordinary axis of the crystal is more easily polarized [due to the birefringent nature of quartz] than the ordinary axes” [2]. When such a particle is positioned in an electric field, a polarization is induced on the particle. Any misalignment between the electric field and the polarization of the particle results in a torque [3]. By monitoring the ellipticity introduced in the trapping beam by this particle, the torque can be determined with great accuracy (typically \sim a few kT).

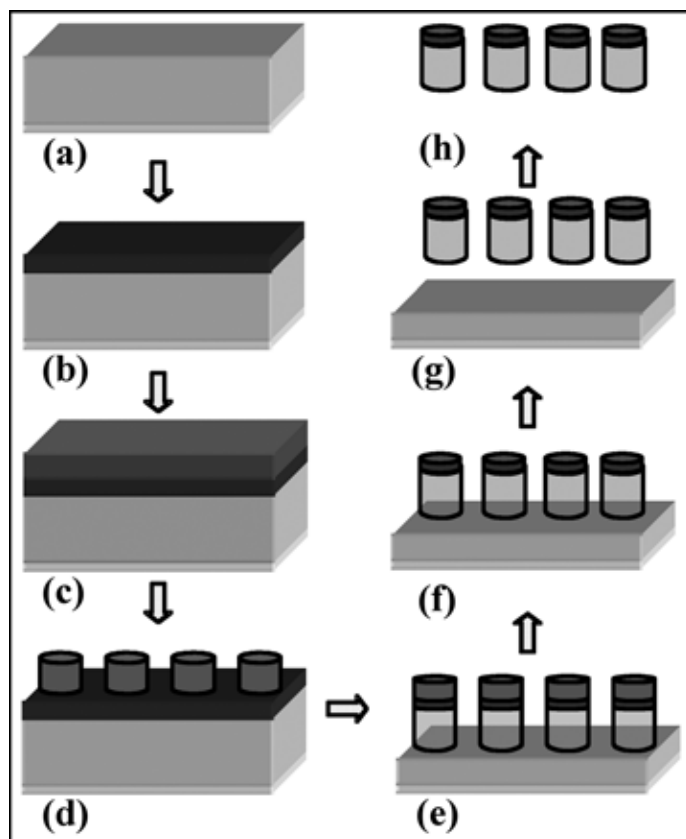


Figure 1: Optimized protocol.

Fabrication

The primary purpose of this project was to master and improve the existing cylindrical nanoparticle fabrication protocols [4]. Figure 1 outlines the optimized fabrication protocol. Part (a) depicts the initial step in our protocol; here a thin anti-reflective coating (ARC) has been applied (this coating was used to prevent unwanted ring like structures from appearing on the wafer from the reflective chucks used in the exposure process). In (b) the top surface has reacted with 3-aminopropyltriethoxysilane (APTES); this is the functionalized area to which we want to attach a biological molecule. Approximately 660 nm of OIR 620-7i has been spun onto the wafer in part (c).

A 10x stepper is used to expose the pattern in (d). Section (e) depicts the first anisotropic dry etch (CHF_3/O_2 used as etching gas). Etching times were selected such that particles of height ~ 1 micron were generated.

In the next step, part (f), the resist is removed by sonicating the cylinders/wafer in an acetone solution. The resist was successfully separated from the cylinder, leaving behind the APTES layer for attachment to streptavidin protein. The cylinders, in section (g), have been cleaved using a microtome blade. Finally, part (h) depicts the end product; from here a sample chamber will be prepared and the localized APTES on the top of the cylinders has to be reacted with streptavidin in order for use in an optical trap.

Summary

A protocol for the production of anisotropic quartz cylinders for use in novel optical trapping experiments was successfully performed with improvements made over the published protocol. Further optimization of the fabrication protocol would involve reducing the overall size of the cylinder. Initial attempts proved challenging due to the optical limits of the nanofabrication tools being reached.

In addition, it may be possible to further refine and improve the trapping handles by employing new particle geometries or perhaps considering alternate fabrication substrates.

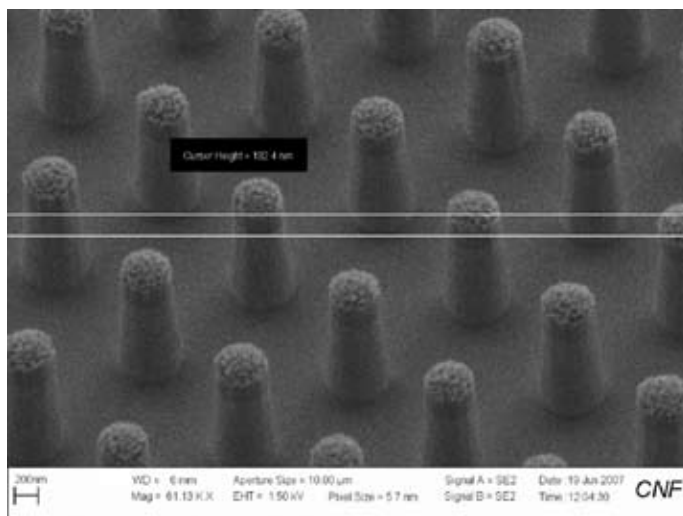


Figure 2, top: Quartz cylinders with resist on top after anisotropic dry etch is performed.

Acknowledgements

I would like to thank my principal investigator, Dr. Michelle Wang, my mentors, Dr. Chris Deufel and Scott Forth, the National Nanotechnology Infrastructure Network Research Experience for Undergraduates Program, the National Science Foundation, and the Cornell NanoScale Facility and staff without which this research would not have been possible.

References

- [1] Svoboda, K., "Biological Applications of Optical Forces," Annual Reviews, <www.annualreviews.org>, 249 (1994).
- [2] La Porta, A. and M.D. Wang, "Optical Torque Wrench: Angular Trapping Rotation and Torque Detection of Quartz Microparticles," Physical Review Letters Volume 92, Number 19 (2003).
- [3] Ibid.
- [4] Deufel, C. et al, "Nanofabricated quartz cylinders for angular optical trapping: torque detection during DNA supercoiling," Nature Methods Vol. 4, 223 (2007).

Investigating Inter-Domain Regulation of von Willebrand Factor Interactions with Platelets

Ryan M. Harrison

Biomedical Engineering & Economics, Johns Hopkins University

NNIN REU Site: Center for Nanotechnology, University of Washington

NNIN REU Principal Investigator: Wendy Thomas, Bioengineering, University of Washington

NNIN REU Mentors: Dr. Shivani Sharma, Dr. AnYue Tu, and Dr. Olga Yakovenko, Bioengineering, University of Washington

Contact: rharrison@jhu.edu, wendyt@u.washington.edu, aytu@u.washington.edu

Abstract/Introduction

Von Willebrand factor (vWF), a large multimeric blood plasma protein, is integral to *in vivo* platelet aggregation and clot formation (Figure1) [1]. Of particular interest are the shear dependent interactions between the A₁-domain of vWF and platelet glycoprotein (GP) Ib_α [2]. Weak, transient bonding between these two partners anchors platelets and vWF long enough for other glycoprotein and integrin mediated bonds to form [3]. Disruption of these transient bonds, such as mutations that abolish the shear dependence of the interaction, lead directly to clinical illnesses such as von Willebrand disease, the most common hereditary blood clotting disorder [1]. To detect the presence of inter-domain regulation within vWF, we investigated the interaction of platelets with the isolated A₁, A₁A₂A₃, D'D₃A₁A₂A₃ and ΔD'D₃ (A₁A₂A₃D₄B₁B₂B₃C₁C₂C_k) domains of vWF under flow conditions. In addition, we conducted ristocetin induced platelet aggregation (RIPA) assays to verify construct functionality, and enzyme linked immunosorbent assays (ELISA) to quantitate construct surface absorption.

Results

ELISA, which were visualized at A₆₅₀ with a horseradish peroxidase (HRP)/HRP antibody system developed by Invitrogen, revealed nonlinear concentration dependence as well as variable coat concentration for the different constructs tested — multimeric vWF, A₁, A₁A₂A₃, D'D₃A₁A₂A₃. Construct size dependent adsorption was observed as expected — A₁ coated at ~24%, A₁A₂A₃ at ~58% and D'D₃A₁A₂A₃ at ~67% of multimeric vWF coating (data not shown).

RIPA assays verified the functionality of the dimeric (D'D₃A₁A₂A₃ and ΔD'D₃), but not monomeric (A₁ and A₁A₂A₃) constructs. RIPA assays rely on the fact that platelets, in combination with ristocetin (antagonist) and a cross linker should aggregate in solution. In Figure 2, our negative control (platelets + vWF) shows no aggregation, while our positive control (platelets + vWF + ristocetin) and dimeric constructs (platelets + construct + ristocetin) aggregate in solution. This reveals that both vWF and dimeric constructs are functionally active in solution; that is,

they bind platelets with high affinity in the presence of a ristocetin antagonist. For monomeric, the paradigm is the opposite—platelets + vWF + ristocetin + monomer should actually inhibit platelet aggregation versus platelets + vWF + ristocetin. No platelet aggregation inhibition was consistently observed, suggesting that our A₁ and A₁A₂A₃ were functionally inactive. This is curious, considering that A₁ is widely known to inhibit platelet aggregation in the presence of ristocetin (or botrocetin, a close analog) [2,4].

Flow chamber experiments were conducted for plates coated with multimeric vWF, A₁, A₁A₂A₃, D'D₃A₁A₂A₃ and ΔD'D₃ in the range of 0.0025 Pa to 16 Pa wall shear stress. Platelet interactions occurred for all constructs other than A₁ and A₁A₂A₃, where the interaction is quantified as the number of platelets bound to the surface in two minutes under flow conditions. Bovine serum albumin (BSA)-coated plates were used as a negative control and a baseline threshold for platelet interactions; that is, constructs

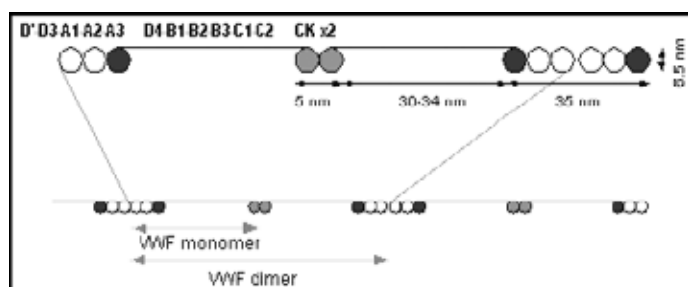


Figure 1: Domain-level structure of von Willebrand factor.

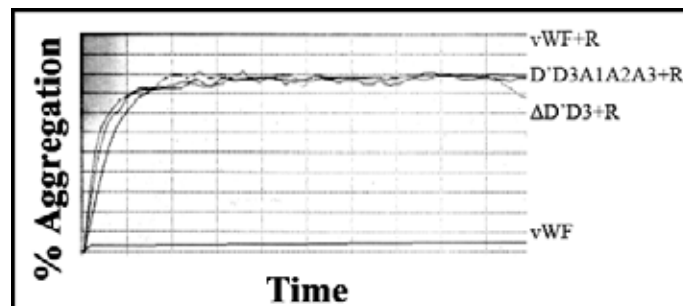


Figure 2: RIPA assay for dimeric vWF constructs.

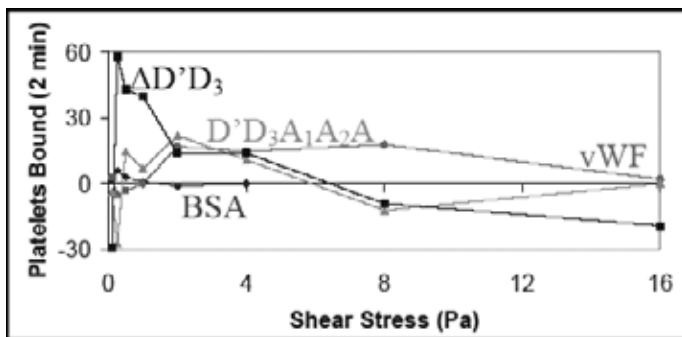


Figure 3: Flow chamber experiment comparing the shear-dependent platelet binding of vWF constructs.

that bound less platelets than BSA, such as A_1 and $A_1A_2A_3$, were considered nonspecific and discounted.

Four experiments were performed in the same conditions on separate days and Figure 3 shows the results from one representative/typical experiment. Note that the $\Delta D'D_3$ construct experiences peak platelet binding at a much lower shear than both multimeric vWF and $D'D_3A_1A_2A_3$. This demonstrates that the $\Delta D'D_3$ domain has a role in regulating the shear dependence of vWF platelet interactions.

Furthermore, at high shear (> 2 Pa), platelets tend to detach from the dimeric constructs while platelet binding occurs throughout the entire high shear range for multimeric vWF.

Methods

Flow chamber experiments were conducted with circular parallel plate flow chambers (Glycotech) following the protocol of Doggett, et. al. 2003 [5]. Variable concentrations of multimeric vWF (Haematologic Technologies Human von Willebrand factor VIII Free, Cat#: HCVWF0191, Stock 210 $\mu\text{g}/\text{mL}$), A_1 , $A_1A_2A_3$, $D'D_3A_1A_2A_3$ and/or $\Delta D'D_3$ were coated onto 35 mm round polystyrene petri dishes (Corning) via a 90 minute incubation at 37°C. Recombinant vWF- A_1 [6] and $A_1A_2A_3$, $D'D_3A_1A_2A_3$ and $\Delta D'D_3$ were prepared and isolated as previously described [7]. vWF construct coated dishes were mounted to the flow chamber, suffused with a platelet rich suspension isolated from healthy donor whole blood and visualized under a 10X light microscope (Nikon) [5]. RIPA assays were conducted following the protocol of Cruz, et. al. 2000 [2].

Conclusion

This study reveals that inter-domain regulation does indeed occur in vWF platelet interactions. Flow chamber experiments demonstrate that the $D'D_3$ domain regulates shear dependent platelet binding by inhibiting low shear vWF platelet interactions by an, as of yet, undetermined mechanism. One possible mechanism is that the $D'D_3$ domain inhibits the A_1 domain at low shear, preventing GP Ib_α binding. However, at high shear, vWF and $D'D_3$ are elongated by shear forces, exposing the A_1 domain.

While in general agreement with our findings, the elongation theory does not explain the discrepancy between the dimeric constructs and vWF platelet binding at high shear. Repeating flow chamber experiments with GP Ib_α coated polystyrene beads instead of intact platelets and characterization under an atomic force microscope are needed to cement our findings as well as to test mechanistic hypotheses.

Acknowledgements

I would like to thank the Lenting Laboratory (University Medical Center Utrecht, Utrecht, the Netherlands) for their generous donation of vWF constructs, Greg Mize (University of Washington, Biochemistry) for agglomerator usage and the Thomas Laboratory for hosting me. Research funded by the National Nanotechnology Infrastructure Network Research Experience for Undergraduates Program and National Science Foundation.

References

- [1] Wagner DD. (1990) An. Rev. Cell. Bio. 6:217242.
- [2] Cruz MA, et. al. (2000) J. Bio. Chem. 275.25:1909819105.
- [3] Doggett TA et. al. (2002) Biophys. J. 83:194–205.
- [4] Fukuda K et. al. (2005) Nature Struct. Mol. Bio. 12:2:152159.
- [5] Doggett TA et. al. (2003) Blood 102:1:152160.
- [6] Cruz MA et. al. (1993) J. Bio. Chem. 268.28:2123821245.
- [7] Ulrichs H et. al. (2006). J. Biol. Chem., 281.8:46994707.

Watershed Segmentation Algorithm for Medical Confocal Image Analyses Towards In Vivo Early Cancer Detection

Man Kin Derek Ho

Department of Biology, Johns Hopkins University

NNIN REU Site: Microelectronics Research Center, The University of Texas at Austin

NNIN REU Principal Investigator: Dr. John X. J. Zhang, Biomedical Engineering, The University of Texas at Austin

NNIN REU Mentor: Karthik Kumar, Electrical Engineering, The University of Texas at Austin

Contact: derekho@jhu.edu, john.zhang@engr.utexas.edu, kkumar@mail.utexas.edu

Abstract

This REU project successfully demonstrated an automated image segmentation technique to overcome artifacts from *in vivo* images and provide real time, accurate analysis of nuclear size, density, and nuclear-cytoplasmic ratio, critical visual markers of epithelial precancers. The algorithm was first calibrated using optical images of microfluidic droplets, and then applied on confocal images of oral cavity tissues. All images were segmented successfully to provide accurate count (95% with 6.2% standard deviation) of cells or droplets.

Introduction

Cancer is a serious global healthcare problem, accounting for over 6.5 million deaths annually. Although widely considered a disease of the developed world, 60% of cancers occur in developing countries, where low per-capita healthcare expenditure, unreliable infrastructure and facilities render advanced cancer screening technologies inaccessible. In lieu of these factors, we have developed a low-cost, handheld, microelectromechanical systems (MEMS)-based *in vivo* confocal microscope for sub-cellular-resolution imaging of tissue towards early detection of epithelial precancers from which 85% of cancers originate. Currently, endoscopic procedures are performed for biopsy samples and images are manually segmented for initial testing of pre-cancer. However, this results in long turnaround time, high costs, discrepancies among different segmentation methods, and

inconvenience for patients. An advanced algorithm is therefore needed to provide fast, low-cost, standardized results which are essential for *in vivo* pre-cancer detection.

Algorithm Outline

The image was imported into MATLAB® and converted to grayscale for faster processing using inbuilt functions. **Imclearborder** was used to eliminate incomplete nuclei and only account for complete and visible ones. The gradient magnitudes were calculated and the threshold was increased to outline cell membranes.

The normal watershed transform usually over-segments so we used the more advanced marker-controlled watershed transform. Foreground objects were marked with local maxima to ensure only wanted objects were accounted for. **Strel** and **graythresh** were used to mark the background in black against the resized white foreground markers. In order to only count minima at

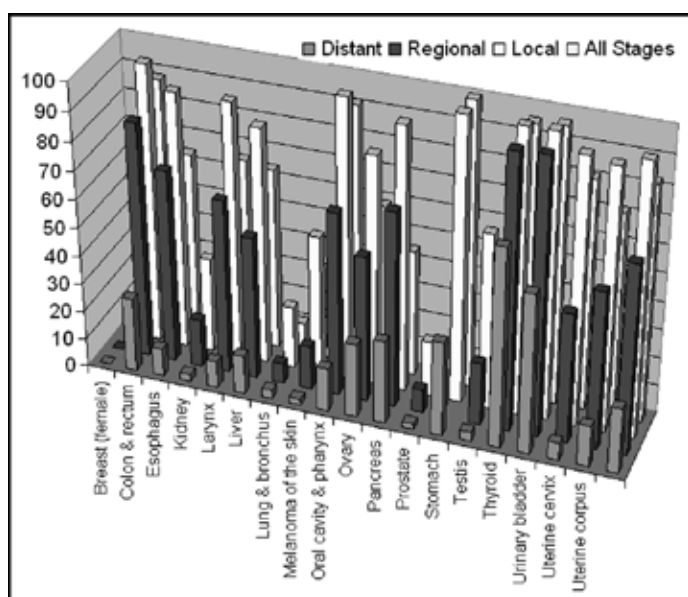


Figure 1: Statistics showing survival rates vs. cancer diagnosed at different stages.

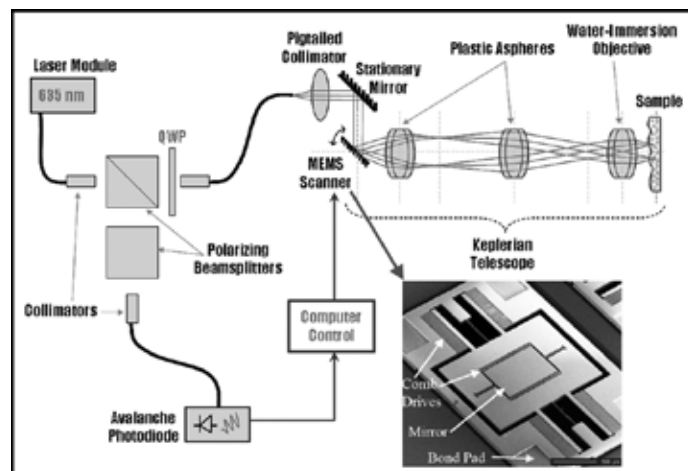


Figure 2: Illustration of our imaging setup with top view of microscanner shown (Inset).

markers and not the entire image, **imimposemin** was used and the transformation was initialized at this point.

To visualize how the watershed function worked, the image was viewed as a topographical surface. The algorithm started at a minima of each marked object and expanded uni-directionally until it reached an edge of another region. The watershed transform was an accurate way to count and segment marked regions. **Bwlabel** labels connected components of the image, which allowed **numObjects** and **Regionprops** to give numerical statistics about the segmented image. Based on results from previous trials, parameters were set up to remove false counts. All nuclei sizes were put into an array and a mean nuclei size was calculated, together with a histogram displaying the occurrences vs. size.

Algorithm Calibration

The algorithm was first calibrated using optical images of droplets in microfluidic channels. Microfluidic channels were fabricated using polydimethylsiloxane (PDMS) with rapid prototyping. A clean silicon wafer was coated with hexamethyldisilazane (HMDS) to ensure good adhesion between silicon and photoresist. Photoresist SU-8 2250 was applied to produce a master of appropriate thickness and the wafer was spun at 1860 rpm for 30 seconds. Under soft lithography, the wafer was exposed to UV light for 50 seconds and developed for 3 minutes. On developing, features of microfluidic channels are transferred to the resist, and the master fabrication is complete. PDMS was poured onto the wafer after applying Sigma-Cote to reduce adhesion between the PDMS and wafer, cured for 45 minutes at 70°C, and peeled to form channels. The master can be used in this manner to reliably reproduce thousands of channels based on a design.

Water droplets dyed with various colors were injected at different arms of the microfluidic channel. The fusion efficiency was observed when different flow rates were applied and the algorithm was capable to segment and count droplets with 93% accuracy and 8.7% standard deviation. Over-segmentation occurred when many droplets did not fuse together. Based on that, an additional criterion was implemented to minimize inaccurately segmented droplets.

Results and Conclusion

Medical confocal images were used for a more rigorous and robust testing of the algorithm. Images were taken from porcine oral cavities with our confocal microscope. The algorithm provided 95% accuracy and 6.2% standard

deviation to hand-segmentation. Although over-segmentation did occur, the mistaken segmented regions were obvious in that they were not nuclei based on size and could therefore be discarded.

The results show that our image segmentation algorithm can analyze images taken *in vivo* and detect nuclei to a good extent. Our algorithm, together with our hand-held *in vivo* microscope, can provide real-time, biopsy-free results.

Future Work

Bayesian Classifiers can be implemented to detect specific object shape and size, which allows an observation of different cancer stages and an idea of what types of treatments are needed. A GUI can be written for easier usage and other research groups can benefit from automated image segmentation versus manual counting. Also with each image there are different objects and signals in them, thus performing a Fourier Transform can be useful in image analysis.

Acknowledgements

I would like to thank the NSF, NNIN Research Experience for Undergraduates Program, Dr. Sanjay Banerjee, NNIN Facility, and Zhang Research Lab at UT Austin.

References

- [1] K. Kumar, K. Hoshino, H.J. Shin, R. Richards-Kortum and X.J. Zhang, "High-reflectivity Two-Axis Vertical Combdrive Microscanners for Sub-cellular Scale Confocal Imaging Applications", Proceedings of International Conference on Optical MEMS and their Applications (Optical MEMS '06), August 21-24, Montana, USA, 2006.
- [2] Brette L. Luck, Kristen D. Carlson, Alan Conrad Bovik, Rebecca R. Richards-Kortum, "An Image Model and Segmentation Algorithm for Reflectance Confocal Images of *In Vivo* Cervical Tissue," IEEE Image Proc., V14, #9, pp. 1265-1276, Sep. 2005.

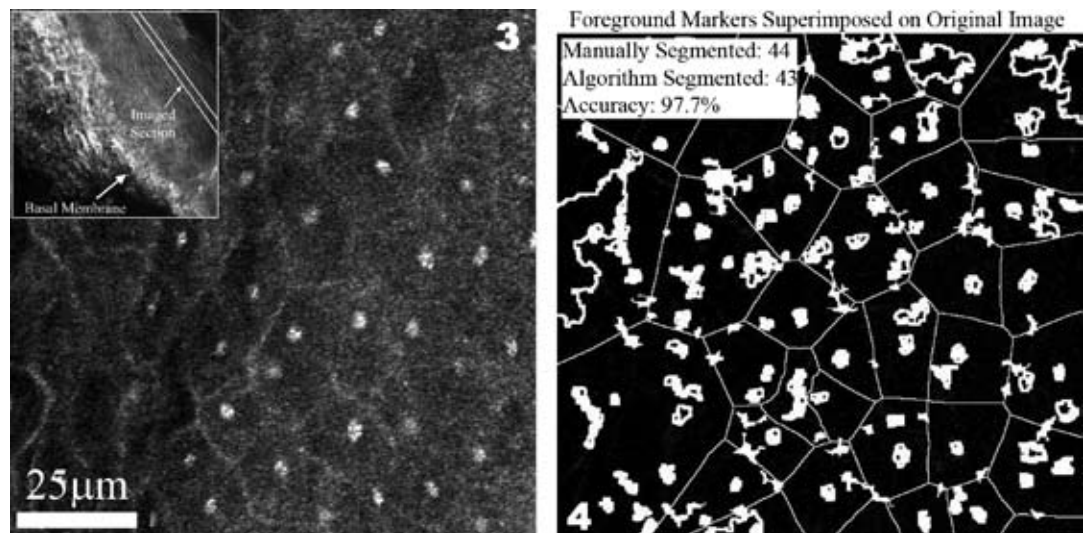


Figure 3: Porcine oral tissue. Inset: Epithelium and basal layer.

Figure 4: Segmented image with markers shown using our algorithm.

Study of Silver Nanoparticles Biocidal Impact on *Escherichia coli* Using Optical and Atomic Force Microscopy

Ruth Enid Kuilan León

Chemical Engineering, University of Puerto Rico, Mayagüez Campus

NNIN REU Site: Howard University Nanoscale Science and Engineering Facility, Howard University

NNIN REU Principal Investigator: Dr. James W. Mitchell, Chemical Engineering, Howard University

NNIN REU Mentor: Dr. Tina Brower-Thomas, Chemical Engineering, Howard University

Contact: rkl21656@uprm.edu, jwm@msrce.howard.edu, tbthomas@msrce.howard.edu

Abstract

Silver's biocidal properties have been known to affect cellular metabolism and inhibit cell growth; therefore it is expected that it will affect *Escherichia coli*, a bacteria known as one of the many species of bacteria living in the lower intestines of mammals. One of the primary adverse effects of the bacteria is the ability to cause food-borne illness. Atomic force microscopy (AFM) is a high-resolution imaging technique that can resolve features as small as an atomic lattice in real space. One of its many advantages is that it allows molecular scale resolution in liquid or without vacuum; therefore it has been immediately extended to biological systems. The focus of the present study was to investigate the structural and surface alterations induced in *E. coli* by the exposure of silver nanoparticles and image these changes using AFM. It is expected we will obtain easily achievable images by AFM with different orientations in space and accurate measurements of the morphology of normal versus affected *E. coli*. Optical microscopy was used for preliminary experiments to confirm that silver nanoparticles can affect the *E. coli* [1-3].

Objective

Investigate the effects induced on *Escherichia coli* when exposed to a biocidal compound such as silver nanoparticles and image them using optical and atomic force microscopy.

Materials and Methods

Surface Characterizations. Silver/silicon (AgSi) and Si wafer samples were studied using AFM. AgSi samples were prepared by DC magnetron sputtering of Ag and Si targets to deposit films onto a Si wafer. The Ag content for the samples was expected to be from 18-20%. Characterization was done by observing patterns on the surface topography and by studying data provided by the AFM, such as the average roughness of each sample. Contact and tapping mode was used, the latter being the ideal method because of its use in biological applications.

Preparation of Bacteria Samples. *E. coli* was grown in two different mediums: brain heart infusion (BHI) broth and nutrient agar. Flame inoculation was used to probe the *E. coli* into glass slants containing each medium. *E. coli* slants were left in an incubator at 37°C overnight to observe bacterial growth. After bacterial growth was evident, slants were labeled as stock solutions.

Serial Dilutions. Phosphate buffer was used to prepare solutions of decreasing bacterial concentration (10^{-1} to 10^{-6}) from *E. coli* BHI stock solution. These were labeled according to their bacterial concentration. The most diluted solutions (10^{-4} to 10^{-6}) were plated in a BHI agar and left to incubate at 37°C overnight to observe and quantify colonies.

Optical Microscopy. *E. coli* BHI stock solution and diluted solutions were observed on depression slides by optical microscopy using a (40x) objective. 500 μ L of each *E. coli* solution were added to the slides with a sterile pipette. *E. coli* behavior was observed and recorded for 5 minutes prior to exposure to silver nanoparticles.

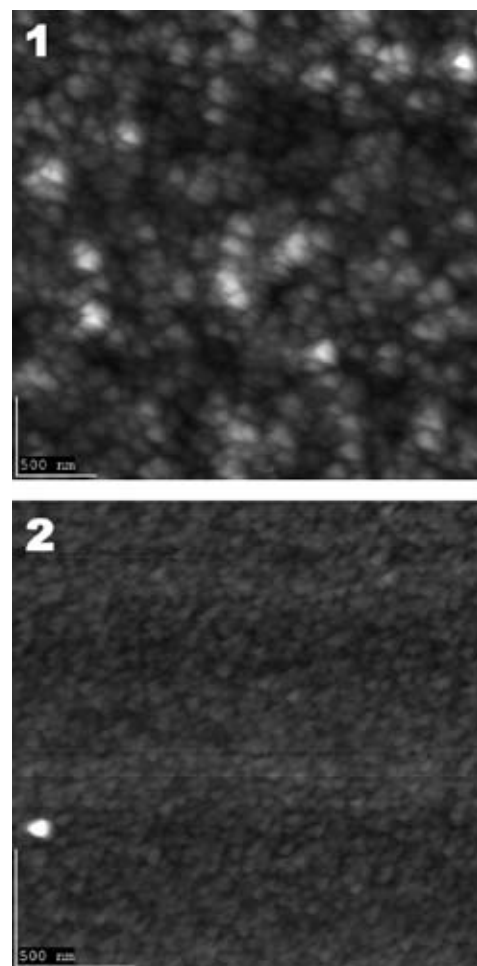


Figure 1, top: AgSi (3 μ m scan) (R_a : 8.27 nm).

Figure 2, bottom: Si (3 μ m scan) (R_a : 0.829 nm).

Silver Nanoparticles. Ag nanoparticle solution was prepared in a RPMI 1640 medium. This solution contained 10^{14} Ag nanoparticles per milliliter. Slides containing *E. coli* were exposed to 200 μ L of Ag nanoparticles solution after 5 minutes of observation. *E. coli* behavior after exposure to Ag nanoparticles was observed for 35 minutes.

Results and Conclusions

Surface Characterization. Different patterns were observed when imaging surfaces by non-contact mode on the AFM. When the Si wafer samples were studied, surface topography images seemed smooth and very uniform contrary to AgSi samples that showed a rougher and more complex surface topography. AgSi samples appeared to have small scattered clusters along the surface. When average roughness (Ra) data was obtained, it showed that Si wafer surfaces had a (Ra = 0.829 nm) and that AgSi samples had a (Ra = 8.27 nm), confirming what was previously observed on surface topography images. Additionally, when the (Ra) for the AgSi sample and Si wafer sample were subtracted, a value of approximately 7 nm was obtained. This value confirmed that silver nanoparticles were embedded in the surface since it was the expected value for the size of the silver nanoparticles when prepared by DC magnetron sputtering. (See Figures 1 and 2.)

***E. coli* and Silver Nanoparticles.** Before silver nanoparticles exposure, *E. coli* seemed healthy and moving freely in solution. *E. coli* was observed for a period of 35 minutes after exposure to silver nanoparticles solutions. During the 35 minute period, the *E. coli* movement began to decrease and *E. coli* began to collide with each other forming clusters. After the 35 minute period, the *E. coli* movement stopped completely and a large number of clusters were observed. (See Figures 3 and 4.)

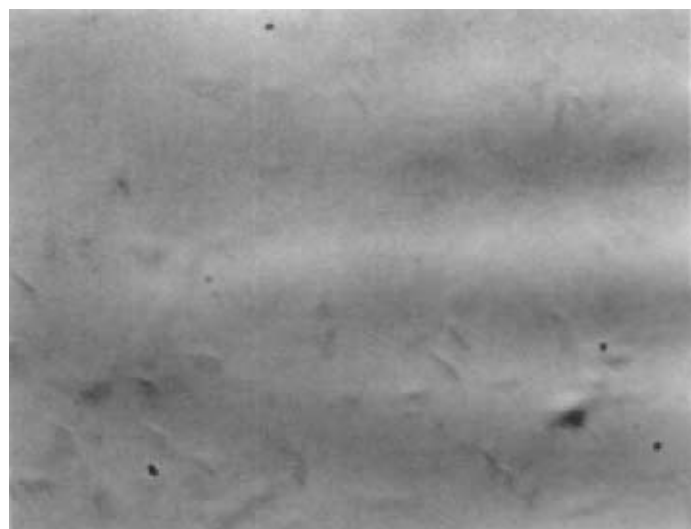


Figure 3: Before exposure to silver nanoparticles.

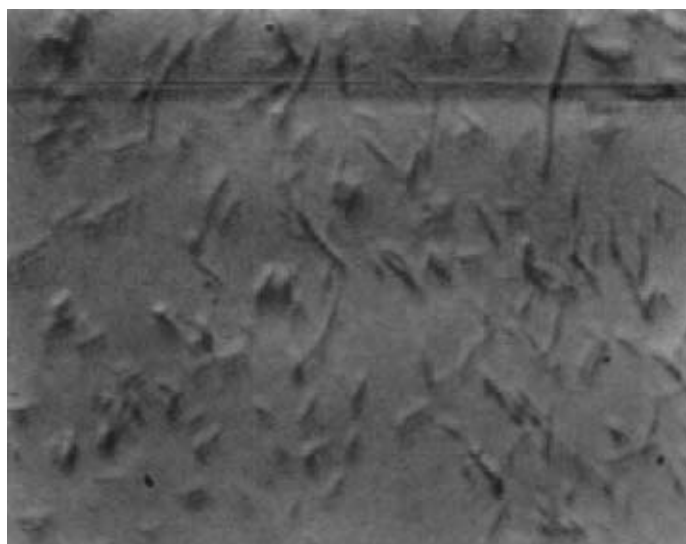


Figure 4: 40 minutes after exposure.

Future Work

Future work is expected to include: further study of surface characterization of AgSi and Si wafer surfaces by AFM, and *E. coli* growth on mica surfaces. In both studies, *E. coli* will be exposed to silver nanoparticles and the *E. coli* behavior will be observed *ex-situ* and *in-situ*, anticipating that it will die. Additionally it is expected that quantifying the *E. coli* in each sample will enable calculation of the rate at which the *E. coli* dies.

Acknowledgements

I thank the National Nanotechnology Infrastructure Network Research Experience for Undergraduates, the National Science Foundation, the CREST Nanomaterials Center, and the Howard Nanoscale and Engineering Facility for the opportunity. Also a special thanks to: Dr. James W. Mitchell, Dr. Tina Brower-Thomas, Mr. James Griffin, Dr. Gary Harris, Dr. Chichang Zhang, Mr. Andy Yuen Hai Ting, Mr. William Rose, and all my new friends at Howard University.

References

- [1] Braga, P.C.; Ricci, D. *Antimicrob. Agents Chemother.* 1998, 42(1), 18-22.
- [2] Doktycz, M.J.; Sullivan, C.J; Hoyt, P.R; Pelletier, D.A.; Wu, S.; Allison, D.P. *Ultramicroscopy.* 2003, 97, 209-206.
- [3] Binnig, G.; Quate, C.F. *Phys. Rev. Lett.* 1985, 56(9), 930-933.

Protein Functionalization of Nanostructured Polymer Surfaces

Ashlee Mangan

Chemistry, Carlow University

NNIN REU Site: Penn State Center for Nanotechnology Education and Utilization, The Pennsylvania State University

NNIN REU Principal Investigator: Dr. Melik C. Demirel, BioNanoMaterials Lab, The Pennsylvania State University

NNIN REU Mentor: Dr. Serhan Boduroglu, BioNanoMaterials Lab, The Pennsylvania State University

Contact: ashlee73184@yahoo.com, mdemirel@enr.psu.edu

Abstract

Immobilization of proteins on polymer surfaces is of great interest for applications in biosensing, cell and tissue culturing, and medical device coating. This research studied the functionalization of a fluorescent protein on a structured polymer surface. Copolymerization of 4-trifluoroacetyl-[2.2]paracyclophane and 4-amino-[2.2]paracyclophane by a vapor deposition technique result in the formation of slanted, columnar, porous structures of the copolymer poly(*o*-trifluoroacetyl-*p*-xylylene-*co*-*o*-amino-*p*-xylylene-*co*-*p*-xylylene), (PPX-COCF₃-NH₂). The coupling of green fluorescent protein (GFP) to the structured and planar (control) polymer surfaces was studied by chemisorption (i.e. using a linking reagent, hexamethylene diisocyanate (HMDI)) and physisorption (i.e. without any linker). The fluorescence intensity of GFP on the surfaces was measured by an optical microscope and the data was analyzed using imaging software. The fluorescence intensity on the structured surfaces was higher than planar surfaces. This method will open a new wealth of applications to functionalize proteins that have desired functional groups for biomedical applications.

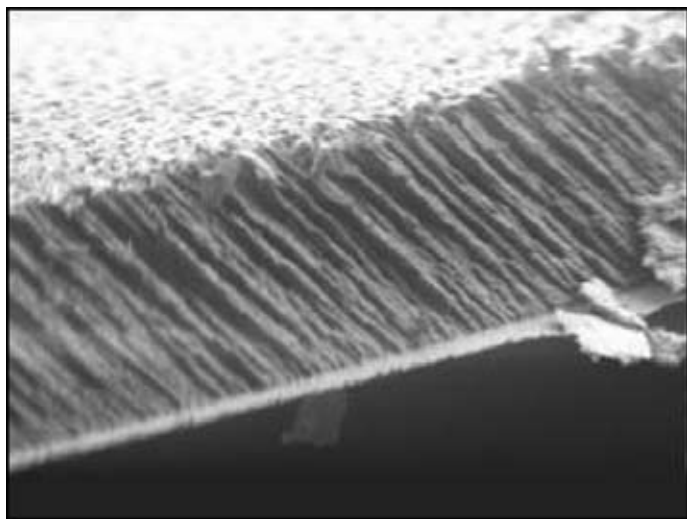


Figure 1: Cross sectional SEM image of a structured PPX film [2].

Introduction

Nanostructured poly(*p*-xylylene) (PPX) films are of great interest because of their unusual physical and chemical properties such as surface chemistry, morphology, and topology [1]. Nanostructured PPX films have increased surface area which enhances the efficiency of functionalization, and this is the significant difference between a planar and structured surface (Figure 1) [2]. Planar surfaces have functional groups only on the top surface whereas structured surfaces have spaces between the columns of porous polymer strands, which provide more functional groups available for attachment to proteins.

Experimental Procedure

Surface functionalization was achieved by placing the films into a flame dried 50 mL round-bottom flask. First 5 mL of anhydrous toluene, 30 μ L of HMDI, and a small amount of catalyst (di-*n*-butyl tin dilaurate) were added to the flask and the top was capped. The reaction was let go for 4 hours. The film was removed from the flask, washed subsequently with toluene and placed in the desiccator to dry for 20 minutes.

GFP coupling to the surfaces was achieved by measuring 5 mL of GFP solution into a 50 mL round-bottom flask. The film in the desiccator was removed, placed into the flask, submerged, and the flask was capped. The reaction was let go overnight. The film was removed from the flask and placed in the desiccator to dry for 20 minutes. The film was removed from the desiccator, washed subsequently with deionized water and placed in the desiccator to dry. The schematic of protein coupling onto a functionalized structured PPX surface is shown in Figure 2.

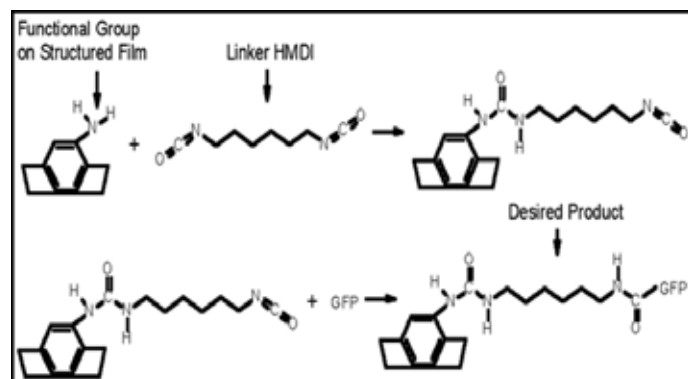


Figure 2: Schematic of protein coupling to PPX surfaces.

GFP imaging was performed using the Olympus Fluoview 300 confocal laser scanning microscope with a single-line 488 nm blue laser using the 40X oil objective. The intensity per field analysis was performed using ImagePro Plus 5.0 [3].

Results and Conclusions

Using the crosslinking agent (HMDI) surface coupling between the reagent and the amino groups on the film was achieved. To characterize the surface of the film, it was run on the FT-IR spectrometer and the resulting spectrum showed 2 peaks that were indicative that the surface coupling reaction linked the amino surface to the coupling reagent (HMDI). The spectra of the unreacted film and HMDI coupled film is shown in Figure 3. The IR spectrum shows an amide bond peak (between 1630-1695 cm^{-1} for the C = O stretching and between 3300-3500 cm^{-1} for a secondary amine). An isocyanate peak at 2200 cm^{-1} is also observed.

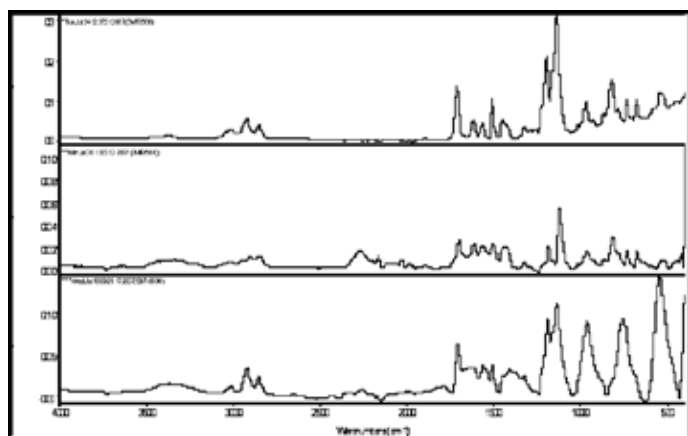


Figure 3: IR spectra: amino film (bottom line), amino film with HMDI (middle line), amino film with GFP (top line) [3].

Next, GFP was attached to the free isocyanate group on the surface. In addition to the fluorescence imaging of PPX surfaces, an IR spectrum confirmed the coupling of GFP to the surface (Figure 3). The spectrum shows that the free isocyanate group has reacted with the GFP.

The GFP intensity was measured in four different conditions using the confocal microscope: (i) a planar PPX-COCF₃-NH₂ surface where the GFP is linked with HMDI (planar-chemisorption); (ii) a structured PPX-COCF₃-NH₂ surface where the GFP is linked with HMDI (structured-chemisorption); (iii) a planar PPX-COCF₃-NH₂ surface where the GFP is adsorbed to the surface without a linker (planar-physisorption); and (iv) a structured PPX-COCF₃-NH₂ surface where the GFP is adsorbed to the surface without a linker (structured-physisorption). The fluorescence intensity results are shown in Figure 4 [3].

Figure 4 shows that nanostructured PPX films have higher intensities compared to planar PPX films. It was also observed

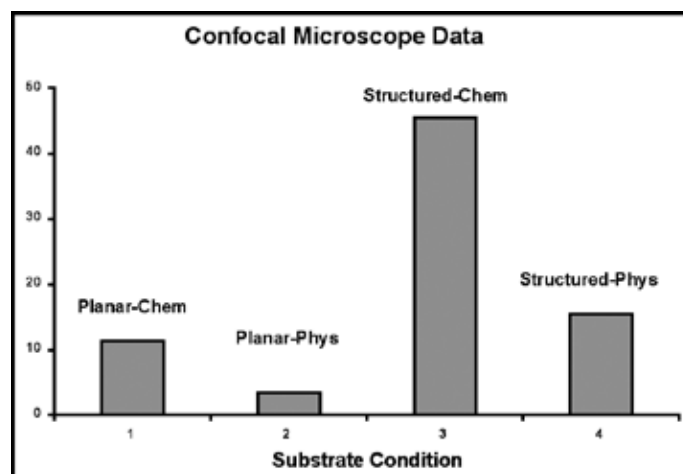


Figure 4: Fluorescence intensity results.

that GFP physisorption on nanostructured PPX films is higher than planar PPX films. This is due to the increased surface area and the porosity of nanostructured PPX films. However, the overall GFP attachment is highest when the GFP is chemisorbed to the nanostructured PPX surface. Novel surface properties can be obtained by coupling reagents attached to the structured PPX film. Therefore, the surface may be incorporated into medical devices or other engineering device applications [3].

Future Work

Another proposal would be to functionalize nanostructured PPX surfaces with RGD peptides, seed cells onto the film and monitor the cell growth. The amino acid sequence of RGD interacts with integrin receptor sites and is found in the extracellular matrix; therefore, it is suggested that cells would be highly attracted to the RGD peptides on the surface and increase cell growth.

Acknowledgments

I would like to thank Dr. Melik C. Demirel, Dr. Serhan Boduroglu, the National Nanotechnology Infrastructure Network REU Program, the NSF, and the Penn State Nanofabrication Facility staff and coordinators.

References

- [1] Cetinkaya, M., Boduroglu, S., Demirel, M.C. "Growth of Nanostructured Thin Films of Poly(p-xylylene) Derivatives by Vapor Deposition", *Polymer*, Vol.48, pg. 4130-4134, (2007).
- [2] Demirel, M.C., Boduroglu S., Cetinkaya, M., Lakhtakia, A. "Spatially Organized Free-Standing Poly(P-xylylene) Nanowires Fabricated by Vapor Deposition", *Langmuir*, Vol. 23, pg. 5861-5863, (2007).
- [3] Mangan, A., Boduroglu, S., Demirel, M.C. "Protein Functionalization of Structured Poly(p-xylylene) Films", *Materials Science and Engineering:C*, submitted, (2007).

Fabrication of a Polymeric Microfluidic Device with Inkjet-Printed Silver Electrodes for Electrokinetic Bioparticle Characterization



Brandon Noia

Biomedical and Electrical and Computer Engineering, Duke University

NNIN REU Site: Cornell NanoScale Science & Technology Facility, Cornell University

NNIN REU Principal Investigator: Prof. Brian Kirby, Mechanical and Aerospace Engineering, Cornell University

NNIN REU Mentor: Benjamin Hawkins, Biomedical Engineering, Cornell University

Contact: brn2@duke.edu, bk88@cornell.edu

Abstract

We are developing an inkjet printing technique for patterning electrodes on polymeric substrates to create microfluidic devices for bioparticle applications. Electrode deposition is important for actuating electrokinetic phenomena in microfluidic devices, and polymeric substrates are becoming increasingly common. Dielectrophoretic (DEP) forces are induced via application of a spatially non-uniform electric field and are directly dependent on the sign and magnitude of the Clausius-Mossotti factor. Accurate characterization of particle response when subject to spatially varying electric fields is essential for successful implementation of DEP-based particle sorting and manipulation techniques. We propose a microfluidic device that will (a) characterize Clausius-Mossotti factors for biologically relevant particles and media, and (b) allow for easy and inexpensive fabrication outside of a clean room environment. Particle characterization is conducted using an interdigitated electrode design in a polymeric microchannel. A Dimatix inkjet printer is used to deposit micro-scale electrodes onto Zeonor 1020R using a silver nano-ink (PChem Assoc.). Electrode resolutions of approximately 70 μm have been accomplished using these techniques, which are compatible with applications on a biological scale. The inkjetting protocols developed allow for fast, inexpensive fabrication of our device and rapid prototyping for future research.

Summary

We are developing inkjet printing techniques for the rapid prototyping and manufacture of polymeric microfluidic devices that require on-device electrodes. Microfluidic devices have been produced utilizing DEP forces for particle sorting [1]. Proper functioning of these devices requires accurate characterization of DEP mobility. We desire a DEP characterization device that is cheap and easy to manufacture outside of a clean room environment. Cyclo-olefin copolymer substrates, such as Zeonor, are ideal for this application since they are inexpensive and mechanically resilient. The deposition of highly conductive electrodes on these substrates is necessary to generate locally non-uniform electric fields.

Dielectrophoretic forces are felt by mobile, polarizable particles subject to spatially-varying electric fields. Analytical modeling of these forces is possible when idealized particles are considered. However, accurate modeling becomes difficult when dealing with biological particles such as cells, which are of non-uniform shape and composition, and are subject to multiple double-layer effects. The magnitude and sign of the DEP force is dependent on the Clausius-Mossotti factor (f_{cm}) (Figure 1). This factor measures the difference in complex permittivity ($\tilde{\epsilon}$) between a particle and a medium in which it is suspended. The complex permittivity is a relation of the permittivity (ϵ) and frequency-dependent conductivity (σ) of a given material. Under a negative DEP force, a particle will be repelled from regions with a high electric field, whereas positive DEP corresponds with movement toward higher electric fields.

$$\langle \bar{F}_{DEP} \rangle = \pi \epsilon_m a^3 \text{Re}[f_{CM}] |\nabla \bar{E}|^2$$

$$f_{CM} = \frac{\tilde{\epsilon}_p - \tilde{\epsilon}_m}{\tilde{\epsilon}_p + 2\tilde{\epsilon}_m}$$

$$\tilde{\epsilon} = \epsilon + \frac{\sigma}{j\omega}$$

Figure 1: Equations for dielectrophoresis and the Clausius-Mossotti factor.

Our proposed device for characterizing DEP mobility relies on interdigitated electrodes crossing a microfluidic channel (Figure 2). The electrodes alternate positive and negative to create a non-uniform electric field. By varying voltage amplitude at a given frequency and known flow rate, a graph of the trapping voltages against drag and sign of the DEP force can be obtained.

Electrode deposition was achieved on Zeonor 1020R using a Dimatix Materials Printer (DMP-2800), a tabletop inkjet printer. To be jettable, an ink must not have large agglomerates of particles or settle quickly, and should have low viscosity and surface tension. Modifications were made to the PFI-300 (PChem Assoc.) silver ink to produce a jetting, conducting ink. The pH of the ink was raised to 5.4 using a solution of 5:1 deionized (DI)

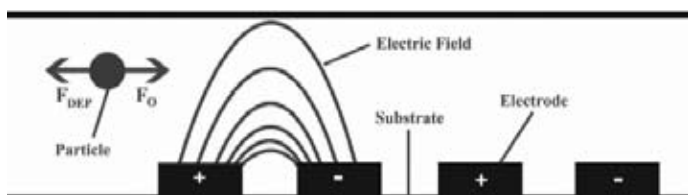


Figure 2: Side view of the proposed dielectrophoretic mobility characterization device, where F_0 denotes Stokes' drag force.

water to ammonium hydroxide, altering interparticle potentials and resulting in smaller aggregations. The ink was then filtered through a $0.8 \mu\text{m}$ filter to remove any remaining large particles. DI water could then be added to increase fluid volume and decrease concentration. Solutions of up to 5:1 DI water to ink were tested, with 1:2 yielding the best results with regards to jettability (Figure 3). The surfactant Triton X-100 was added in small amounts to later inks prior to filtering, which resulted in better electrode conductivity. A ratio of 40:1 Triton X-100 to ink resulted in the most effective jetting while maintaining conductivity.

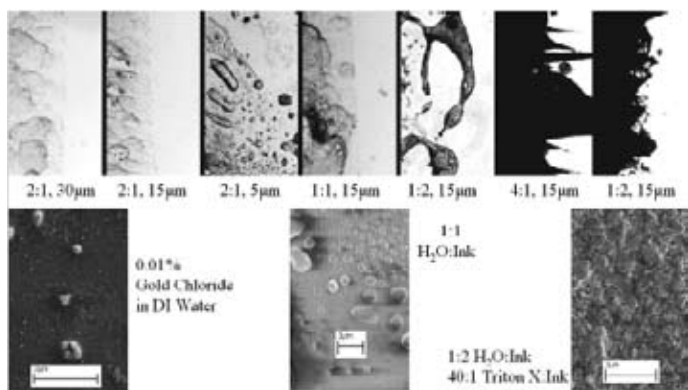


Figure 3: Various inks printed on a Zeonor 1020R substrate given in ratio of DI water to ink.

The Dimatix inkjet printer had to be tuned for functional ink jetting. Even after filtering, particle settling and ink evaporation resulted in clogging at the nozzle head. A 0.1 second purge cycle, during which a pressure increase forcefully pushed ink through the nozzles, was run every 300 seconds to remove clogs and keep the ink fresh. No heat was applied to the nozzle or to the Zeonor substrate, and voltage amplitudes were adjusted specifically for each nozzle.

Using these techniques and materials, we were able to produce promising results. Conductive silver electrodes were successfully printed onto a Zeonor substrate. We were only able to resolve the printed silver features down to about 1 mm. This was due in part to some variability in the angle at which the silver droplets would leave the print head. We hope to be able to produce smaller resolutions in the future. The device has been printed on paper using a model ink with $90 \mu\text{m}$ resolution (Figure 4), which is sufficient to actuate DEP forces in biological

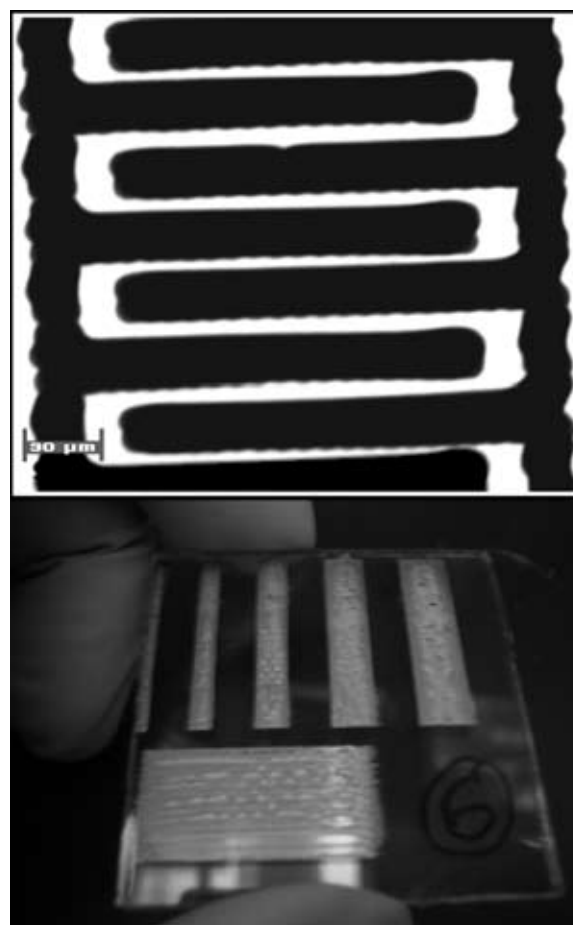


Figure 4: Top; High resolution printing of DEP characterization device with model ink on paper. Bottom; The electrodes printed on Zeonor, with researcher's hand for scale. The electrodes all conduct along their entire length and are of different widths. The far left is 1mm wide.

particles. Electrode adherence to the Zeonor substrate has been tested with several solvents, including ethanol, isopropyl alcohol, and acetone. Adherence can be improved by depositing a 3-Mercaptopropyltrimethoxysilane monolayer onto the Zeonor substrate prior to electrode printing, though this is necessary only if the electrodes are subject to relatively large mechanical stresses. We believe that our inkjet manufacturing techniques will allow electrode-based microfluidic devices to be easily produced, paving the way for future rapid prototyping applications.

Acknowledgements

Benjamin Hawkins and Brian Kirby for their guidance and support. The National Nanotechnology Infrastructure Network Research Experience for Undergraduates Program, National Science Foundation, and the Intel Foundation for funding. All the staff and faculty at the Cornell NanoScale Facility.

References

- [1] Hawkins, B.G., Smith, A.E., Syed, Y.A., and Kirby, B.J., *Anal. Chem.*, 2007.

Three-Dimensional Flow-Focusing in Microfluidic Devices



Sasha Perkins

Materials Science and Engineering, University of Florida

NNIN REU Site: Cornell NanoScale Science & Technology Facility, Cornell University

NNIN REU Principal Investigator: Dr. Carl Batt, Department of Food Science, Cornell University

NNIN REU Mentors: Matthew Kennedy, Electrical Engineering, Cornell University;

Clarissa Lui, Biomedical Engineering, Cornell University

Contact: splerks@ufl.edu, cab10@cornell.edu, mjk67@cornell.edu, csl42@cornell.edu

Introduction

Over the recent years, an interest in hand-held devices applicable in forensics and biological applications which need fast and efficient data analysis has increased through the research of lab-on-a-chip systems and bead-based detection technology [1]. In this research, three-dimensional hydrodynamic flow-focusing has been obtained in a two layer polydimethylsiloxane (PDMS) microfluidic device. Using sheath flow, this device employs a microfluidic manifold to focus fluorescent particles in three dimensions ensuring that the particles will be confined to the focal volume of the optical fibers embedded into the deoxyribonucleic acid (DNA) analysis microchip. The flow-focusing performance of this device has been characterized as a prelude to its integration into a hand-held particle-counter microchip. The geometry of the inputs and liquids of different viscosities were tested in order to achieve the most effectively focused stream. Through laser scanning confocal microscopy, the focused stream, using polyvinyl alcohol as a sheath fluid, was found to have a width of about $15\ \mu\text{m}$ and a height of about $25\ \mu\text{m}$. In addition, successful calcium cross linking of sodium alginate microfibrils was seen in this device with confocal microscopy through the diffusion of sheath fluid into the focused stream, within a channel of $100\ \mu\text{m}$ by $100\ \mu\text{m}$ cross section.

Experimental Procedure

The microfluidic device was constructed through two layer soft lithography [2]. Channels of $100\ \mu\text{m}$ depth and $100\ \mu\text{m}$ width were fabricated by spinning SU-8 100 photoresist onto blank silicon wafers at 2900 rpm for 35s. The distance between the inlets in the patterns did not affect the focused stream as much as the dimensions of the actual channels. After spinning the resist on the silicon wafers, the wafers were pre-baked for 10 min at 65°C and then soft-baked for 30 min at 95°C . The wafers were exposed to ultraviolet light through a patterned chrome mask at $600\ \text{mJ}/\text{cm}^2$ for 8s, three times. The exposed wafers were then baked for 10 min at 95°C [3]. After developing the wafer, polydimethylsiloxane (PDMS) was poured on the patterned silicon wafers and cured in an oven for 2 hr at 60°C . After curing the PDMS, the two layers of PDMS were placed into an oxygen plasma asher and then aligned under a contact aligner. Polyethylene tubing was attached to the inlets and outlets of the flow cell with epoxy. A final product of a flow cell, seen in Figure 1, shows the flow cell before being characterized.

Different geometries and different solutions of various viscosities, such as ethylene glycol, glycerol, Tris-HCL with EDTA (TE buffer), and polyvinyl alcohol were tested as sheath fluid and sample flow solutions to see the size and location of the focused stream with the fluorescent beads. The rate of the syringe pump was also considered. The velocity of the beads on the focused stream was also calculated to see how fast the beads could be detected. The focused stream was characterized under a Leica confocal microscope.

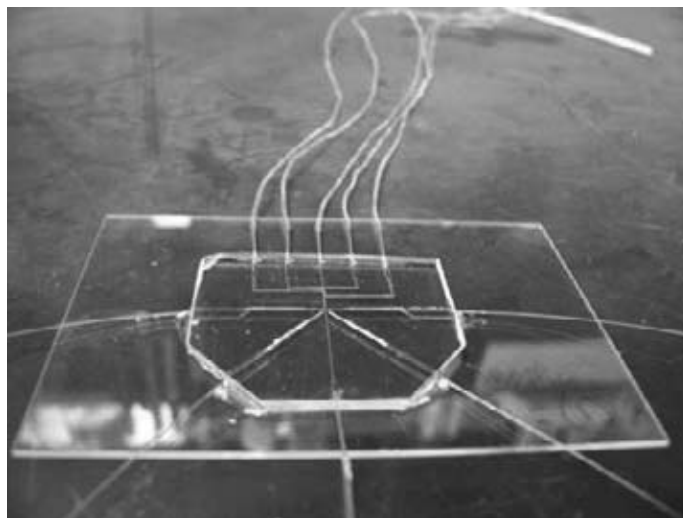


Figure 1: Assembled flow cell with channels that have a cross section of $100\ \mu\text{m}$ by $100\ \mu\text{m}$.

Results and Conclusions

The most effective pattern was designed with a symmetrical setting with the sheath fluid channels joining the central channel from both sides and from the top and shortly after, sheath fluid would connect from both sides and the bottom as shown in Figure 2. The dimensions of the side sheath fluid channels were $50\ \mu\text{m}$ wide, while the central channel was $100\ \mu\text{m}$ wide. TE buffer

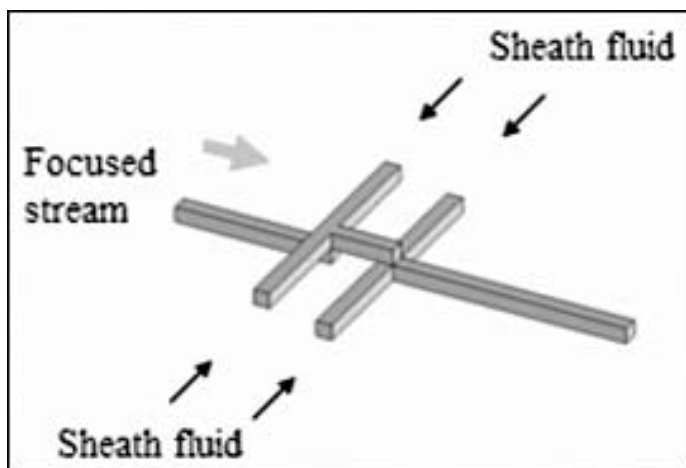


Figure 2: Schematic drawing of flow cell with 50 μm wide central channel and 100 μm wide sheath fluid channels.

(with 80% glycerol to increase its viscosity) was used to carry the sample and flowed at 3 $\mu\text{l}/\text{min}$. (TE buffer is commonly used as a buffer for DNA.) Polyvinyl alcohol was pumped as sheath fluid at 13 $\mu\text{l}/\text{min}$. This version provided a focused stream with a width of about 15 μm and a height of about 25 μm in the center of the central channel as shown in Figure 3. A more circular focused stream was characterized because the side channels did not provide high pressure in the central channel which would cause the focused stream to be more oblong.

The velocity of 5 μm -in-diameter fluorescent beads was about 10 $\text{cm}/\text{s} \pm 2 \text{ cm}/\text{s}$ in the focused stream. The velocity of the beads was calculated based on 20 streak-length measurements using pixel size and the rate at which the images were scanned. Also, due to the diffusion caused in the central channel in the flow cells designed, alginate microfibers were fabricated using sodium alginate in the sample flow and calcium chloride as sheath fluid. The sample flow was pumped at 1 $\mu\text{l}/\text{min}$ and the sheath fluid was pumped at 333 $\mu\text{l}/\text{min}$ [4].

Future Work

Particles need to be analyzed to test the usability of the microfluidic device, by attaching the optical fibers in the microchip. Some work was done during this research to create bioluminescent microfibers using Renilla Luciferase in the sample flow and adding coelenterazine substrate to the microfibers after making them in the flow cell. However, the glow was not able to be seen.

Acknowledgements

Intel Foundation, National Nanotechnology Infrastructure Network, Cornell NanoScale Science and Technology Facility, National Science Foundation, Dr. Carl Batt, Matthew Kennedy, and Clarissa Lui.

References

- [1] Gardeniers, J. G. E, et al. "Lab-on-a-chip systems for biomedical and environmental monitoring", Analytical and Bioanalytical Chemistry, Vol.378, Number 7, Pages 1700-1703 (April 2004).
- [2] Sundararajan, N. et al. "Three-Dimensional Hydrodynamic Focusing in Polydimethylsiloxane (PDMS) Microchannels", Journal of Microelectromechanical Systems, Volume 3, No. 4, Pages 559-568 (August 2004).
- [3] "NanoTM SU-8." MicroChem. Rev 2/02. http://microchem.com/products/pdf/SU8_50-100.pdf
- [4] Shin, S et al. "On the Fly Continuous Generation of Alginate Fibers Using a Microfluidic Device", June 6, 2007. Langmuir 2007, 23, 9104-9108, ACS Publications. Retrieved from <http://pubs.acs.org/cgi-bin/article.cgi/langd5/2007/23/i17/pdf/la700818q.pdf>.

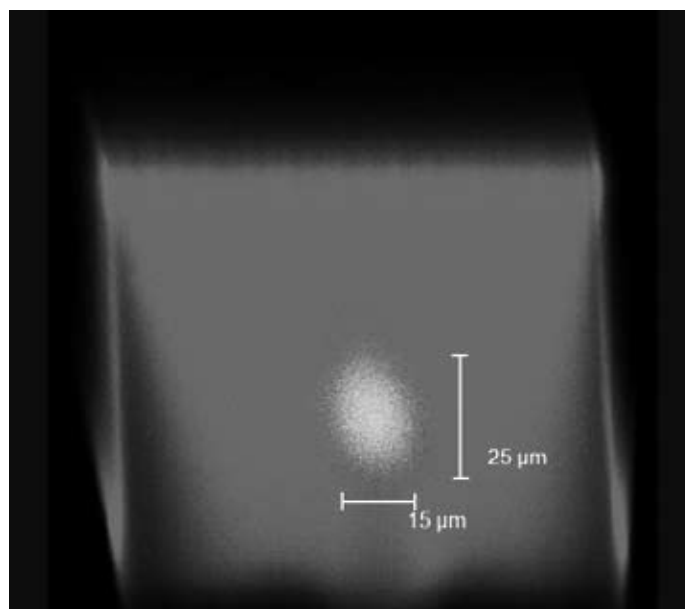


Figure 3: Cross-section view of focused stream under confocal microscope. The focused stream had a 25 μm height and a 15 μm width.